Monthly Notices
of the
ROYAL ASTRONOMICAL SOCIETY

MNRAS **462,** 1864–1881 (2016)
Advance Access publication 2016 July 20

doi:10.1093/mnras/stw1749

Dark-matter haloes and the M–σ relation for supermassive black holes

Adam C. Larkin★ and Dean E. McLaughlin★

Astrophysics Group, Lennard-Jones Laboratories, Keele University, Keele, Staffordshire ST5 5BG, UK

Accepted 2016 July 17. Received 2016 July 17; in original form 2015 September 9

ABSTRACT

We develop models of two-component spherical galaxies to establish scaling relations linking the properties of spheroids at $z = 0$ (total stellar masses, effective radii R_e and velocity dispersions within R_e) to the properties of their dark-matter haloes at both $z = 0$ and higher redshifts. Our main motivation is the widely accepted idea that the accretion-driven growth of supermassive black holes (SMBHs) in protogalaxies is limited by quasar-mode feedback and gas blow-out. The SMBH masses, M_{BH}, should then be connected to the dark-matter potential wells at the redshift z_{qso} of the blow-out. We specifically consider the example of a power-law dependence on the maximum circular speed in a protogalactic dark-matter halo: $M_{BH} \propto V_{d,pk}^4$, as could be expected if quasar-mode feedback were momentum-driven. For haloes with a given $V_{d,pk}$ at a given $z_{qso} \geq 0$, our model scaling relations give a typical stellar velocity dispersion $\sigma_{ap}(R_e)$ at $z = 0$. Thus, they transform a theoretical M_{BH}–$V_{d,pk}$ relation into a prediction for an observable M_{BH}–$\sigma_{ap}(R_e)$ relation. We find the latter to be distinctly non-linear in log–log space. Its shape depends on the generic redshift evolution of haloes in a Λ cold dark matter cosmology and the systematic variation of stellar-to-dark matter mass fraction at $z = 0$, in addition to any assumptions about the physics underlying the M_{BH}–$V_{d,pk}$ relation. Despite some clear limitations of the form we use for M_{BH} versus $V_{d,pk}$, and even though we do not include any SMBH growth through dry mergers at low redshift, our results for M_{BH}–$\sigma_{ap}(R_e)$ compare well to data for local early types if we take $z_{qso} \sim 2$–4.

Key words: galaxies: bulges – galaxies: elliptical and lenticular, cD – galaxies: fundamental parameters – galaxies: haloes – quasars: supermassive black holes.

1 INTRODUCTION

The masses M_{BH} of supermassive black holes (SMBHs) at the centres of normal early-type galaxies and bulges correlate with various global properties of the stellar spheroids – see Kormendy & Ho (2013) for a comprehensive review. The strongest relationships include one between M_{BH} and the bulge mass M_{bulge} (either stellar or dynamical, depending on the author; e.g. Magorrian et al. 1998; Marconi & Hunt 2003; Häring & Rix 2004; McConnell & Ma 2013); a scaling of M_{BH} with the (aperture) stellar velocity dispersion σ_{ap} averaged inside some fraction of the effective radius R_e of the bulge ($M_{BH} \sim \sigma_{ap}^{4-5}$ if fitted with a single power law; Ferrarese & Merritt 2000; Gebhardt et al. 2000; Ferrarese & Ford 2005; McConnell & Ma 2013); and a fundamental-plane dependence of M_{BH} on a combination of either M_{bulge} and σ_{ap} or σ_{ap} and R_e (Hopkins et al. 2007b,c). Whether any one correlation is more fundamental than the others is something of an open question (see e.g. Shankar et al. 2016, who suggest σ is more fundamental), but collectively they are interpreted as evidence for co-evolution between SMBHs and their host galaxies.

This co-evolution likely involved self-regulated feedback in general. Most of the SMBH mass in large galaxies is grown in a quasar phase of Eddington-rate accretion (Yu & Tremaine 2002), driven by a rapid succession of gas-rich mergers at high redshift. Such accretion deposits significant momentum and energy back into the protogalactic gas supply, which can lead to a blow-out that stops further accretion on to the SMBH. In this context, the empirical correlation between M_{BH} and σ_{ap} takes on particular importance, as the stellar velocity dispersion should reflect the depth of the potential well from which SMBH feedback had to expel the protogalactic gas. Cosmological simulations of galaxy formation now routinely include prescriptions for the quenching of Eddington-rate accretion by 'quasar-mode' feedback, with free parameters that are tuned to give good fits to the SMBH M–σ relation at $z = 0$.

However, it is not clear in detail how the stellar velocity dispersions in normal galaxies at $z = 0$ relate to the protogalactic potential wells when any putative blow-out occurred and the main phase of accretion-driven SMBH growth came to an end. For most systems, this was presumably around $z \sim 2$–3, when quasar activity in the Universe was at its peak (Richards et al. 2006; Hopkins, Richards & Hernquist 2007a). The potential wells in question were dominated by dark matter, and a general method is lacking to connect the stellar σ_{ap} in spheroids to the properties of their dark-matter

★ E-mail: a.larkin@keele.ac.uk (ACL); d.e.mclaughlin@keele.ac.uk (DEM)

haloes, not only at $z = 0$ but at higher redshift as well. Moreover, it is not necessarily obvious what specific property (or properties) of dark-matter haloes provides the key measure of potential-well depth in the context of a condition for accretion-driven blow-out. Different simulations of galaxy and SMBH co-evolution with different recipes for quasar-mode feedback appear equally able (with appropriate tuning of their free parameters) to reproduce the observed M–σ relation.

Our main goal in this paper is to address the first part of this problem. We develop 'mean-trend' scaling relations between the average stellar properties (total masses, effective radii and aperture velocity dispersions) and the dark-matter haloes (virial masses and radii, density profiles and circular-speed curves) of two-component spherical galaxies. These scalings are constrained by some data for a representative sample of local early-type galaxies, and by the properties of dark-matter haloes at $z = 0$ in cosmological simulations. We then include an analytical approximation to the mass and potential-well growth histories of simulated dark-matter haloes, in order to connect the stellar properties at $z = 0$ to halo properties at $z > 0$. We ultimately use these results to illustrate how one particularly simple analytical expression, which gives a critical SMBH mass for protogalactic blow-out directly in terms of the dark-matter potential well at quasar redshifts, translates to a relation between SMBH mass and stellar velocity dispersion at $z = 0$.

1.1 SMBH masses and halo circular speeds

Under the assumption (which we discuss just below) that accretion feedback is momentum-conserving and takes the form of a spherical shell driven outwards by an SMBH wind with momentum flux $\mathrm{d}p_{\rm wind}/\mathrm{d}t = L_{\rm Edd}/c$, McQuillin & McLaughlin (2012) derive a minimum SMBH mass sufficient to expel an initially static and virialized gaseous medium from any protogalaxy consisting of dark matter and gas only. This critical mass is approximately

$$M_{\rm BH} \simeq \frac{f_0\kappa}{\pi G^2}\frac{V_{\rm d,pk}^4}{4} \simeq 1.14\times10^8\ {\rm M}_\odot \left(\frac{f_0}{0.2}\right)\left(\frac{V_{\rm d,pk}}{200\ {\rm km\ s^{-1}}}\right)^4, \quad (1)$$

where κ is the Thomson-scattering opacity and f_0 is the (spatially constant) gas-to-dark matter mass fraction in the protogalaxy. The velocity scale $V_{\rm d,pk}$ refers to the *peak* value of the circular speed $V_{\rm d}^2(r) \equiv GM_{\rm d}(r)/r$ in a dark-matter halo with mass profile $M_{\rm d}(r)$. Equation (1) holds for any form of the mass profile, just so long as the associated circular-speed curve has a single, global maximum – as all realistic descriptions of the haloes formed in cosmological N-body simulations do. Defining a characteristic (dark-matter) velocity dispersion as $\sigma_0 \equiv V_{\rm d,pk}/\sqrt{2}$ turns equation (1) into a critical $M_{\rm BH}$–σ_0 relation, which is formally the same as that obtained by King (2003, 2005), and similar to the earlier result of Fabian (1999), for momentum-driven blow-out from a singular isothermal sphere.

This critical mass is based on the simplified description given by King & Pounds (2003) of a Compton-thick wind resulting from accretion at or above the Eddington rate on to an SMBH. In particular, their analysis provides the assumption that the momentum flux in the SMBH wind is simply $L_{\rm Edd}/c$ (with no pre-factor).[1] The wind from an SMBH with mass greater than that in equation (1) will then supply an outward force (i.e. $L_{\rm Edd}/c = 4\pi GM_{\rm BH}/\kappa$) on a thin, radiative shell of swept-up ambient gas that exceeds the gravitational attraction of dark matter behind the shell (maximum force $f_0V_{\rm d,pk}^4/G$ if the gas was initially virialized), *everywhere* in the halo. It is a condition for the clearing of all gas to beyond the virial radius of any non-isothermal halo.

Equation (1) has limitations. Most notably, the protogalactic outflows driven by SMBH winds are in fact expected to become energy-driven (non-radiative) after an initial radiative phase (Zubovas & King 2012; McQuillin & McLaughlin 2013). This may (Silk & Rees 1998; McQuillin & McLaughlin 2013) or may not (Zubovas & Nayakshin 2014) change the functional dependence of a critical $M_{\rm BH}$ for blow-out on the dark-matter $V_{\rm d,pk}$ or any other characteristic halo velocity scale. Beyond this, the equation also assumes a wind moving into an initially static ambient medium, ignoring the cosmological infall of gas and an additional, confining ram pressure that comes with hierarchical (proto-)galaxy formation (Costa, Sijacki & Haehnelt 2014). It also neglects the presence of any stars in protogalaxies, which could contribute both to the feedback driving gaseous outflows (e.g. Murray, Quataert & Thompson 2005; Power et al. 2011) *and* to the gravity containing them. [The assumptions of spherical symmetry and a smooth ambient medium are not fatal flaws; see Zubovas & Nayakshin (2014).]

However, it is not our intention here to improve equation (1). Rather, we aim primarily to establish a method by which halo properties at $z > 0$ in relations *such as* equation (1) can be related to the average properties of stellar spheroids at $z = 0$. By doing this, we hope to understand better how expected relationships between SMBH masses and protogalactic dark-matter haloes are reflected in the observed M–σ relation particularly. Equation (1) is a good test case because it is simple and transparent but still contains enough relevant feedback physics to be interesting, even with the caveats mentioned above. It is also the only such relation we know of, which does not assume that dark-matter haloes are singular isothermal spheres.

1.2 Halo circular speeds and stellar velocity dispersions

As a point of reference, Fig. 1 shows SMBH mass against the stellar velocity dispersion $\sigma_{\rm ap}(R_{\rm e})$ within an aperture equal to the stellar effective radius, for galaxies and bulges in the compilation of McConnell & Ma (2013). The dashed line shows equation (1) evaluated with a gas-to-dark matter mass ratio of $f_0 = 0.18$ (the cosmic average; Planck Collaboration XVI 2014) for all protogalaxies at the time of blow-out, and with the naive substitution $V_{\rm d,pk} \equiv \sqrt{2}\,\sigma_{\rm ap}(R_{\rm e})$ for all spheroids at $z = 0$. The proximity of this line to the data –first emphasized by King (2003, 2005), who assumed isothermal haloes – encourages taking seriously the basic physical ideas behind equation (1), even though (as discussed above) some details must be incorrect at some level.

However, setting $V_{\rm d,pk} = \sqrt{2}\,\sigma_{\rm ap}(R_{\rm e})$ is problematic. A $\sqrt{2}$-proportionality between circular speed and velocity dispersion is appropriate only for isothermal spheres, which real dark-matter haloes are not. A dark-matter velocity dispersion can be equated to a stellar velocity dispersion only if the dark matter and the stars have the same spatial distribution, which is not true of real galaxies. And $V_{\rm d,pk}$ in equation (1) refers to a protogalactic halo, which will have grown significantly since the quasar epoch at $z \sim 2$–3.

[1] Having $\mathrm{d}p_{\rm wind}/\mathrm{d}t = L_{\rm Edd}/c$, rather than $\propto L_{\rm Edd}/c$ but much less, implies high wind speeds of up to $\sim 0.1\,c$ (King 2010). Such ultrafast outflows are observed in many local active galactic nuclei and low-redshift quasars accreting at or near their Eddington rates (e.g. Pounds et al. 2003; Reeves, O'Brien & Ward 2003; Tombesi et al. 2010, 2011).

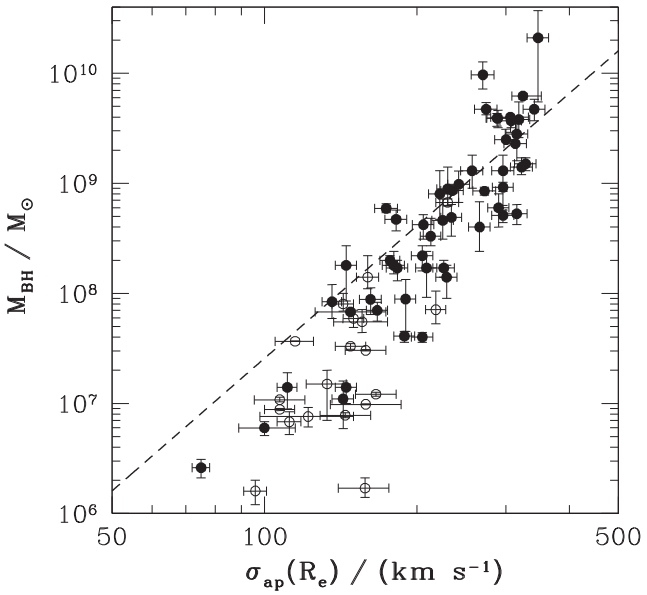

Figure 1. SMBH mass versus stellar velocity dispersion averaged over an effective radius. Data are from the compilation of McConnell & Ma (2013) for 53 E or S0 galaxies (filled circles) and 19 bulges in late Hubble types (open circles). The dashed line is equation (1) with a protogalactic gas-to-dark matter fraction $f_0 = 0.18$ and $V_{\rm d,pk} \equiv \sqrt{2}\,\sigma_{\rm ap}(R_{\rm e})$ for all galaxies. Improving upon this poorly justified association between the characteristic stellar and dark-matter velocities in early-type galaxies is one of the goals of this paper.

In Section 2, we gather results from the literature that we need in order to address these issues. In Section 3, we combine them to constrain simple models of spherical, two-component galaxies, focusing on scaling relations between the stellar and dark-matter properties at $z = 0$. This is done without any reference to black holes, and the scalings should be of use beyond applications to SMBH correlations. In Section 4, we make a new, more rigorous comparison of equation (1) to the SMBH M–σ data (compare Fig. 6 below to Fig. 1). Our work could in principle be used to explore the consequences of SMBH–halo relations like equation (1) for other SMBH–bulge correlations as well, but we do not pursue these here. In Section 5, we summarize the paper.

2 MODEL INGREDIENTS

Equation (1) incorporates an assumption that gas traced the dark matter in *protogalaxies* before being blown out by quasar-mode accretion feedback at high redshift. However, it does not make any assumptions about the detailed structure of dark-matter haloes at any epoch, and it neither requires nor implies that mass follows light in galaxies at $z = 0$.

In this section, we collect together analytical expressions from the literature for the (different) stellar and dark-matter mass profiles in galaxies, and for some key structural parameters of dark-matter haloes and their evolution in Λ cold dark matter (ΛCDM) simulations of structure formation. We use these to obtain our new results in Sections 3 and 4. Some of these expressions from the literature, and all of the scaling relations we ultimately derive, represent average trends that can have significant scatter around them. We do not attempt in this paper to analyse such scatter or to predict the net scatter around any scaling that comes from combining others.

This section and Section 3 do not rely on any ideas about black hole accretion feedback or SMBH–bulge correlations. We focus repeatedly on the peak circular speed $V_{\rm d,pk}$ in dark-matter haloes, because that is what appears in equation (1) for $M_{\rm BH}$; but we do not actually use the equation until Section 4.

2.1 Stellar distribution

We use the spherical density profile of Hernquist (1990) to describe the stars in early-type galaxies at $z = 0$. The density in this model can be written in terms of the total stellar mass, $M_{*,\rm tot}$, and the effective radius, $R_{\rm e}$:

$$\frac{\rho_*(r)}{M_{*,\rm tot}/R_{\rm e}^3} = \frac{\mathscr{R}^2}{2\pi}\left(\frac{r}{R_{\rm e}}\right)^{-1}\left[1+\mathscr{R}\left(\frac{r}{R_{\rm e}}\right)\right]^{-3}, \tag{2}$$

where the constant $\mathscr{R} \simeq 1.815\,27$ (see Hernquist 1990). The mass profile, $M_*(r) = \int_0^r 4\pi u^2 \rho_*(u)\,{\rm d}u$, is then

$$\frac{M_*(r)}{M_{*,\rm tot}} = \left[\frac{r/R_{\rm e}}{r/R_{\rm e}+1/\mathscr{R}}\right]^2. \tag{3}$$

Integrating the Hernquist $\rho_*(r)$ along the line of sight gives a surface density profile that closely approximates the classic $R^{1/4}$ law. Thus, it adequately represents the typical light distributions in spheroids of mass $M_{*,\rm tot} \sim 10^{10}$–$10^{12}\,{\rm M}_\odot$, which more generally follow Sérsic (1968) profiles – $I(R) \sim \exp\,[-(R/R_{\rm e})^{1/n}]$ – with indices $n \approx 3$–7 (e.g. see Graham & Colless 1997). These stellar masses correspond to velocity dispersions $\sigma_{\rm ap}(R_{\rm e}) \sim 80$–$350\,{\rm km\,s^{-1}}$ (see Fig. 4), which is the range spanned by the local galaxies that define the black hole M–σ relation in Fig. 1.

The fine details of the assumed stellar density or mass profile matter most in our calculations of dimensionless stellar velocity dispersions $\sigma_{\rm ap}(R_{\rm e})/\sqrt{GM_{*,\rm tot}/R_{\rm e}}$ using the Jeans equation with model dark-matter haloes included (see Section 3.5 below). Secondarily, the exact shape of $\rho_*(r)$ affects the mass ratio $M_*(r_{\rm vir})/M_*(R_{\rm e})$, which we discuss in Section 3.4. We examine closely in Section 3 the consequences of using Hernquist profiles for all galaxies in our calculations. In general, it exposes us to possible errors at the $\sim$10 per cent level or less.

2.2 Dark-matter distributions

Since the dark-matter circular speed $V_{\rm d,pk}$ enters equation (1) through a high power, it is important that we have a good idea of how sensitive our results may be to the details of the dark-matter density profile that we assume. We therefore consider four different models for spherical haloes. Each of these is a two-parameter model defined by a mass scale and a radial scale. To treat them uniformly, it is most convenient to normalize all radii to the point r_{-2} where the logarithmic slope of the dark-matter density is ${\rm d}\ln\rho_{\rm d}/{\rm d}\ln r = -2$. Masses are then normalized to the mass enclosed within $r < r_{-2}$.

First, the usual NFW profile (Navarro, Frenk & White 1996, 1997) has density

$$\rho_{\rm d}(r) \propto \left(\frac{r}{r_{-2}}\right)^{-1}\left(1+\frac{r}{r_{-2}}\right)^{-2}, \tag{4}$$

which yields the mass profile

$$\frac{M_{\rm d}(r)}{M_{\rm d}(r_{-2})} = \frac{\ln(1+r/r_{-2}) - (r/r_{-2})(1+r/r_{-2})^{-1}}{\ln(2)-1/2}. \tag{5}$$

The circular-speed curve of the halo *alone*, i.e. $V_{\rm d}^2(r) = GM_{\rm d}(r)/r$, is then given by

$$\frac{V_{\rm d}^2(r)}{V_{\rm d}^2(r_{-2})} = \frac{\ln(1+r/r_{-2}) - (r/r_{-2})(1+r/r_{-2})^{-1}}{(r/r_{-2})\,[\ln(2)-1/2]}, \tag{6}$$

which peaks at the radius

$$\frac{r_{\rm pk}}{r_{-2}} \simeq 2.16258. \tag{7}$$

The second model is that of Hernquist (1990), which was first fitted to simulated dark-matter haloes by Dubinski & Carlberg (1991). This has the same central density cusp ($\rho_{\rm d} \to r^{-1}$) as an NFW halo, but a steeper large-radius slope ($\rho_{\rm d} \to r^{-4}$ rather than r^{-3}) and hence a finite, rather than divergent, total mass. When written in terms of r_{-2} and $M(r_{-2})$ rather than the effective radius and total mass, the model is

$$\rho_{\rm d}(r) \propto \left(\frac{r}{r_{-2}}\right)^{-1} \left(1+\frac{1}{2}\frac{r}{r_{-2}}\right)^{-3} \tag{8}$$

and

$$\frac{M_{\rm d}(r)}{M_{\rm d}(r_{-2})} = 9\left(\frac{r/r_{-2}}{2+r/r_{-2}}\right)^2, \tag{9}$$

giving a circular-speed curve,

$$\frac{V_{\rm d}^2(r)}{V_{\rm d}^2(r_{-2})} = \frac{9\,r/r_{-2}}{(2+r/r_{-2})^2}, \tag{10}$$

with a peak at radius

$$\frac{r_{\rm pk}}{r_{-2}} = 2. \tag{11}$$

The third model is one from the family developed by Dehnen & McLaughlin (2005), which reproduces the universal power-law behaviour of 'pseudo' phase-space density profiles, $\rho_{\rm d}(r)/\sigma_{\rm d}^3(r)$, in simulated dark-matter haloes. This model fits the resolved parts of the density profiles alone better than either the NFW or Hernquist profiles, and about as well as the Einasto (1965) density profiles with $\rho_{\rm d}(r) \sim \exp(-r^{\alpha})$, first advocated in this context by Graham et al. (2006). The Dehnen & McLaughlin density is

$$\rho_{\rm d}(r) \propto \left(\frac{r}{r_{-2}}\right)^{-7/9} \left[1+\frac{11}{13}\left(\frac{r}{r_{-2}}\right)^{4/9}\right]^{-6}. \tag{12}$$

This has a slightly shallower central cusp than the NFW or Hernquist profiles and a large-radius fall-off, $\rho_{\rm d} \to r^{-31/9}$, which is steeper than NFW (resulting in a finite total halo mass) but shallower than Hernquist. The mass profile is then

$$\frac{M_{\rm d}(r)}{M_{\rm d}(r_{-2})} = \left[\frac{24\,(r/r_{-2})^{4/9}}{13+11\,(r/r_{-2})^{4/9}}\right]^5 \tag{13}$$

and the circular-speed curve is

$$\frac{V_{\rm d}^2(r)}{V_{\rm d}^2(r_{-2})} = \left[\frac{24\,(r/r_{-2})^{11/45}}{13+11\,(r/r_{-2})^{4/9}}\right]^5, \tag{14}$$

which reaches its peak value at

$$\frac{r_{\rm pk}}{r_{-2}} = \left(\frac{13}{9}\right)^{9/4} \simeq 2.28732. \tag{15}$$

Finally, the halo model of Burkert (1995) has a constant-density core that appears more suited to the dynamics of some low-mass galaxies (e.g. Burkert & Silk 1997), and a large-radius fall-off that is the same as NFW. Here, the density is

$$\rho_{\rm d}(r) \propto \left(1+\mathscr{R}\frac{r}{r_{-2}}\right)^{-1} \left(1+\mathscr{R}^2\frac{r^2}{r_{-2}^2}\right)^{-1}, \tag{16}$$

with $\mathscr{R} \simeq 1.521\,38$. The corresponding mass profile is

$$\frac{M_{\rm d}(r)}{M_{\rm d}(r_{-2})} = \frac{\ln[(1+\mathscr{R}r/r_{-2})\sqrt{1+\mathscr{R}^2\,(r/r_{-2})^2}\,] - \tan^{-1}(\mathscr{R}r/r_{-2})}{\ln[(1+\mathscr{R})\sqrt{1+\mathscr{R}^2}\,] - \tan^{-1}(\mathscr{R})}, \tag{17}$$

which gives a circular-speed curve,

$$\frac{V_{\rm d}^2(r)}{V_{\rm d}^2(r_{-2})} = \frac{\ln[(1+\mathscr{R}r/r_{-2})\sqrt{1+\mathscr{R}^2\,(r/r_{-2})^2}\,] - \tan^{-1}(\mathscr{R}r/r_{-2})}{(r/r_{-2})\left\{\ln[(1+\mathscr{R})\sqrt{1+\mathscr{R}^2}\,] - \tan^{-1}(\mathscr{R})\right\}}, \tag{18}$$

that peaks at

$$\frac{r_{\rm pk}}{r_{-2}} \simeq 2.13433. \tag{19}$$

Fig. 2 shows the circular-speed curves of these haloes, from equations (6), (10), (14) and (18). Relative to the NFW profile, the Hernquist curve has a narrower width overall because of its steeper decline beyond the peak, which follows from its steeper density profile and convergent mass as $r \to \infty$. The Burkert $V_{\rm d}^2(r)$ profile is much narrower because of its steeper rise from small r,

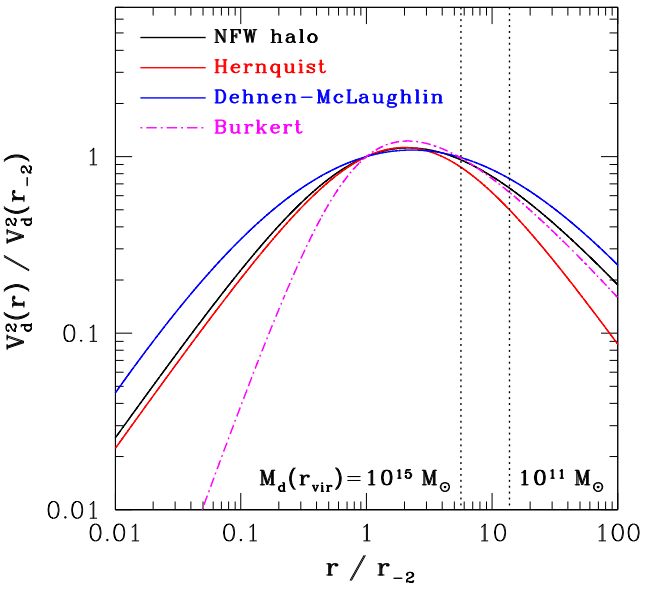

Figure 2. Normalized circular-speed curves, $V_{\rm d}^2(r) = GM_{\rm d}(r)\big/r$, for the four dark-matter halo models we consider. The radius r_{-2} is that where the local density slope is $\mathrm{d}\ln\rho_{\rm d}/\mathrm{d}\ln r = -2$. The peaks in $V_{\rm d}(r)$ occur at radii near $r_{\rm pk}/r_{-2} \approx 2$ in all cases (see the text). Broken vertical lines show the concentrations $r_{\rm vir}/r_{-2}$ of haloes with virial masses $M_{\rm d}(r_{\rm vir}) = 10^{15}$ and $10^{11}\,{\rm M}_\odot$ at $z = 0$ (see Section 2.5). The different widths of the circular-speed curves for the different haloes lead to different values for the baryon fraction inside a stellar effective radius (which is typically in the range $R_{\rm e}/r_{-2} \sim 0.02$–$0.1$; see Section 3), as well as different ratios $V_{\rm d,pk}/\sigma_{\rm ap}(R_{\rm e})$.

which is a result of its having a constant-density core rather than a central density cusp. The Dehnen & McLaughlin (2005) halo has the broadest circular-speed curve overall, largely because of how slowly its density profile (which depends on $r^{4/9}$ rather than just r) rolls over from its central cusp with $\rho_{\rm d}(r) \sim r^{-7/9}$ to its power-law behaviour $\rho_{\rm d}(r) \sim r^{-31/9}$ at large radii. In the analysis of Section 3, these features ultimately affect not only the ratio $V_{\rm d,pk}/\sigma_{\rm ap}(R_{\rm e})$, but also the self-consistent value of $M_*(R_{\rm e})/M_{\rm d}(R_{\rm e})$, the stellar mass fraction inside the effective radius.

2.3 Stellar-to-dark matter mass ratios

The global ratio of stellar to dark-matter mass in galaxies is a strong and non-monotonic function of halo mass that changes with redshift. Behroozi, Wechsler & Conroy (2013) compare several derivations of this function at $z \approx 0$ by different groups using different methods. In this paper, we adopt a parametrization from Moster et al. (2010).

Moster et al. assign one central galaxy to each virialized halo (which might be a subhalo within a larger structure having its own central galaxy) in ΛCDM simulations of structure formation with $\Omega_{m,\,0} = 0.26$, $\Omega_{\Lambda,0} = 0.74$ and $H_0 = 72\,{\rm km\,s^{-1}\,Mpc^{-1}}$. The stellar mass of any central galaxy is determined by the virial mass of its parent halo according to a prescription that is required ultimately to give agreement between the simulations and the observed galaxy luminosity function. They fit their results, for the central-galaxy mass fraction $M_*/M_{\rm d}$ within the virial radius $r_{\rm vir}$ at $z = 0$, with a double power-law function:

$$\frac{M_*(r_{\rm vir})}{M_{\rm d}(r_{\rm vir})} = 0.0564 \left\{ \left[\frac{M_{\rm d}(r_{\rm vir})}{7.66\times10^{11}\,{\rm M}_\odot} \right]^{-1.06} + \left[\frac{M_{\rm d}(r_{\rm vir})}{7.66\times10^{11}\,{\rm M}_\odot} \right]^{+0.556} \right\}^{-1} \qquad (20)$$

(see their equation 2 and their table 6). We discuss the virial radii themselves in the next subsection. Stellar mass fractions inside any other radius follow self-consistently from specifications of the stellar and dark-matter density profiles, as Section 3 will detail.

Equation (20) represents an average trend; scatter around it can be expected, for example, as a result of differences in the merger histories of haloes with the same mass at $z = 0$. Moster et al. (2010) and Behroozi et al. (2013) show that the relation is in good overall agreement with other theoretical work and/or with data, for halo virial masses $10^{11}\,{\rm M}_\odot \lesssim M_{\rm d}(r_{\rm vir}) \lesssim 10^{15}\,{\rm M}_\odot$. This corresponds to stellar masses $5\times10^{8}\,{\rm M}_\odot \lesssim M_*(r_{\rm vir}) \lesssim 10^{12}\,{\rm M}_\odot$ for the central galaxies. The brightest galaxies used to define the observed M–σ relation are at the upper end of this range.

Equation (20) does not attempt to account for the total baryonic mass within the virial radius of any halo; it is only for stellar mass, and only that concentrated at the centre. There will be significantly more baryonic mass in large (cluster-sized) haloes especially, in the form of intracluster light and X-ray gas, and in the stars of galaxies inside virialized subhaloes. We discuss this further in Section 3 and conclude that the complication of additional baryons can safely be ignored for our purposes.

2.4 Virial radii and cosmological parameters

We use the fitting formula of Bryan & Norman (1998, see their equation 6) to calculate the overdensity, relative to the critical density, of a virialized sphere at redshift z in a flat universe with a cosmological constant ($\Omega_m + \Omega_\Lambda = 1$):

$$\Delta_{\rm vir}(z) \equiv \frac{2\,G M(r_{\rm vir})}{H^2(z)\,r_{\rm vir}^3} \simeq 18\pi^2 \;-\; 82\,\frac{1-\Omega_{m,0}}{[H(z)/H_0]^2} \;-\; 39\,\frac{\left(1-\Omega_{m,0}\right)^2}{[H(z)/H_0]^4}, \qquad (21)$$

with

$$\left[\frac{H(z)}{H_0}\right]^2 = 1 \;+\; \Omega_{m,0}[(1+z)^3 - 1]. \qquad (22)$$

Rearranging the definition of $\Delta_{\rm vir}$ yields a convenient relationship between virial radius and virial mass at arbitrary redshift:

$$\left[\frac{M(r_{\rm vir})}{{\rm M}_\odot}\right]\left[\frac{r_{\rm vir}}{\rm kpc}\right]^{-3} \;=\; 1166.1\,h_0^2\,\Delta_{\rm vir}(z)\left[\frac{H(z)}{H_0}\right]^2, \qquad (23)$$

where $h_0 \equiv H_0/(100\ {\rm km\,s^{-1}\,Mpc^{-1}})$ as usual. This form is also useful for calculating M/r^3 of spheres with other overdensities Δ besides the virial value [e.g. $\Delta(z) \equiv 200$].

Whenever we use any of equations (21)–(23), we take cosmological parameters from the *Planck* 2013 results (Planck Collaboration XVI 2014): $h_0 = 0.67$ with $\Omega_{m,0} = 0.32$ (which includes a baryon density of $\Omega_{b,0} = 0.049$) and $\Omega_{\Lambda,0} = 0.68$.

2.5 Halo concentrations

By the concentration of a dark-matter halo, we specifically mean the ratio of $r_{\rm vir}$ [within which, the mean overdensity is given by equation (21)] to r_{-2} (where the slope of the density profile is $\mathrm{d}\ln\rho_{\rm d}/\mathrm{d}\ln r = -2$). It is also common in the literature to define concentration as the ratio of r_{200} (within which, the mean overdensity is $\Delta = 200$) to r_{-2}. Either way, N-body simulations of CDM structure formation consistently show that, at least for low redshifts, more massive haloes have lower concentrations on average. We need to take account of this in order to infer the location and the value of the maximum circular speed in any dark-matter halo with a given virial radius and mass.

Dutton & Macciò (2014) give a fitting formula for the concentrations $r_{\rm vir}/r_{-2}$ of simulated haloes with masses $10^{11}\,{\rm M}_\odot \lesssim M_{\rm d}(r_{\rm vir}) \lesssim 10^{15}\,{\rm M}_\odot$ at redshifts $0 \le z \le 5$ in a *Planck* cosmology. Namely,

$$\log\left[\frac{r_{\rm vir}}{r_{-2}}\right] \simeq a \;-\; b\log\left[\frac{M_{\rm d}(r_{\rm vir})}{10^{12}\,h_0^{-1}\,{\rm M}_\odot}\right] \qquad (24)$$

with

$$a = 0.537 + 0.488\exp(-0.718\,z^{1.08})$$
$$b = 0.097 - 0.024\,z.$$

Again, we set $h_0 = 0.67$ whenever we use this equation. Simulated haloes scatter around the average trend at the level of a few tens of per cent in $r_{\rm vir}/r_{-2}$ for a fixed virial mass and redshift (Bullock et al. 2001; Dutton & Macciò 2014).

Dutton & Macciò obtain equation (24) by fitting NFW density profiles to their simulated haloes in order to measure the radius r_{-2}. They also investigate the use of Einasto (1965) profiles instead [which are more like the Dehnen & McLaughlin (2005) haloes that we explore] to fit for r_{-2} in estimating the alternative concentration r_{200}/r_{-2}. Their results suggest that concentration values depend on the choice of model for the dark-matter density profile, but only at the $\lesssim$10 per cent level for haloes with $M_{\rm d}(r_{\rm vir}) \gtrsim 10^{12}\,{\rm M}_\odot$ at $z = 0$. We apply equation (24) in

our models regardless of what model we assume for $\rho_{\rm d}(r)$ and simply accept that there is a modest uncertainty associated with doing so.

The two vertical lines in Fig. 2 show the concentrations according to equation (24) for haloes with virial masses at $z = 0$ of $M_{\rm d}(r_{\rm vir}) = 10^{11}$ M$_\odot$ (having $r_{\rm vir}/r_{-2} = 13.8$) and 10^{15} M$_\odot$ (having $r_{\rm vir}/r_{-2} = 5.64$). Equation (20) gives the corresponding stellar masses of the central galaxies as $M_*(r_{\rm vir}) = 6.3 \times 10^8$ and 1.0×10^{12} M$_\odot$. This emphasizes the degree to which $V_{\rm d,pk}$ – the key predictor of self-limited SMBH masses in the simple feedback model behind equation (1) – reflects conditions far outside the stellar distributions of normal galaxies (generally, $R_{\rm e}/r_{-2} \sim 0.02$–$0.1$; see Section 3).

Equation (24) has been derived from simulations of strictly baryon-free haloes. This is not an issue for our modelling, precisely because the equation describes haloes on large scales $r > r_{-2} \gg R_{\rm e}$, well away from any regions that might have been altered significantly by the presence of stars.

2.6 Halo progenitors

If the central black hole in a protogalaxy ended its main, quasar phase of accretion growth at a redshift $z > 0$, with a mass $M_{\rm BH}$ determined by the circular speed $V_{\rm d,pk}$ in the dark-matter halo at that time, then we need to relate that earlier $V_{\rm d,pk}$ to the value at $z = 0$ (in order ultimately to link it and $M_{\rm BH}$ to a stellar velocity dispersion at $z = 0$).

From N-body simulations and merger trees of ΛCDM haloes with virial masses at $z = 0$ in the range 10^{11} M$_\odot \lesssim M_{\rm d,vir}(0) \lesssim 10^{15}$ M$_\odot$, van den Bosch et al. (2014) extract for each halo the redshift $z_{1/2}$ at which its *most massive progenitor* had a virial mass $M_{\rm d,vir}(z_{1/2}) = 0.5\,M_{\rm d,vir}(0)$. Given the bottom-up nature of structure formation in CDM cosmologies, $z_{1/2}$ is a decreasing function of $M_{\rm d,vir}(0)$ in general. We have fitted the median dependence shown in fig. 4 of van den Bosch et al. with the function

$$z_{1/2} \;=\; 2.05 \left[\frac{M_{\rm d,vir}(0)}{10^{12}\,h_0^{-1}\,{\rm M}_\odot}\right]^{-0.055} - 1, \qquad (25)$$

again taking $h_0 = 0.67$ from the *Planck* cosmology. Once again, there is intrinsic scatter around this overall trend.

Given $z_{1/2}$, we then approximate the virial mass of the most massive progenitor of a halo at any other redshift by the exponential function (see also, e.g., Zhao et al. 2009),

$$\frac{M_{\rm d,vir}(z)}{M_{\rm d,vir}(0)} = \exp\left[-\frac{\ln(2)}{z_{1/2}}z\right]. \qquad (26)$$

Equations (25) and (26) together give curves of $M_{\rm d,vir}(z)/M_{\rm d,vir}(0)$ versus $M_{\rm d,vir}(0)$ that, for redshifts $z \lesssim 5$, compare well to the curves plotted by van den Bosch et al. (2014) directly from the simulations they analyse (e.g. see their fig. 2).

To obtain the evolution of the peak circular speed in the most massive progenitor of a halo, we first write (for any z)

$$\frac{V^2_{\rm d,pk}}{V^2_{\rm d,vir}} \equiv \frac{V^2_{\rm d}(r_{\rm pk})}{V^2_{\rm d}(r_{\rm vir})} \;=\; \frac{g(r_{\rm pk}/r_{-2})}{g(r_{\rm vir}/r_{-2})}, \qquad (27)$$

where $g(r/r_{-2})$ is one of the normalized circular-speed curves shown in Fig. 2 and written on the right-hand sides of equations (6), (10), (14) and (18) above. Then, since the ratio $r_{\rm pk}/r_{-2}$ is independent of redshift (it is fixed by assuming a basic form for the dark-matter density profile), we have

$$\begin{aligned}\frac{V^2_{\rm d,pk}(z)}{V^2_{\rm d,pk}(0)} &= \frac{g[(r_{\rm vir}/r_{-2})_{z=0}]}{g[(r_{\rm vir}/r_{-2})_z]} \times \frac{V^2_{\rm d,vir}(z)}{V^2_{\rm d,vir}(0)} \\ &= \frac{g[(r_{\rm vir}/r_{-2})_{z=0}]}{g[(r_{\rm vir}/r_{-2})_z]} \\ &\quad \times \left[\frac{M_{\rm d,vir}(z)}{M_{\rm d,vir}(0)}\right]^{2/3} \left[\frac{\Delta_{\rm vir}(z)}{\Delta_{\rm vir}(0)}\right]^{1/3} \left[\frac{H(z)}{H_0}\right]^{2/3}, \qquad (28)\end{aligned}$$

where the last line uses the fact that $V^2_{\rm d}(r) \propto M_{\rm d}(r)/r$ and brings in equation (23). For any choice of dark-matter halo model, and thus of the function $g(r/r_{-2})$, the right-hand side of equation (28) is known in terms of z and $M_{\rm d,vir}(0)$, via equations (25) and (26) plus equations (21), (22) and (24).

The upper panel of Fig. 3 shows the virial masses at $z = 1, 3$ and 5, relative to the $z = 0$ virial masses, for the most massive progenitors of haloes spanning the range of $M_{\rm d,vir}(0)$ investigated by van den Bosch et al. (2014). The middle panel shows the masses of the largest progenitors at $z = 1, 3$ and 5 directly as functions of the halo mass at $z = 0$. The curves in these plots are the same for any model of the halo density profile. The lower panel of Fig. 3 shows the ratio of progenitor to present $V_{\rm d,pk}$ at $z = 1, 3$ and 5 against the $z = 0$ virial mass, calculated using equation (28). These curves depend on the halo density profile. For clarity, we only show results assuming either a Dehnen & McLaughlin (2005) or a Hernquist (1990) density profile, so $g(r/r_{-2})$ is given either by equation (14) or by equation (10).

It is worth noting here the gradual flattening towards higher masses of the curves for $M_{\rm d,vir}(z)$ versus $M_{\rm d,vir}(0)$ in the middle panel of Fig. 3, and how the flattening sets in at more modest halo masses for larger z. This is a generic feature of structure formation by hierarchical merging. Haloes in any given mass range at $z = 0$ have progenitors drawn from increasingly narrow mass ranges, on average, at increasingly high redshift, and this narrowing is more pronounced as a function of z for higher mass haloes, because more of their growth has occurred more recently.

Precise numbers – such as the possible value of a maximum mass for the largest progenitors suggested by the $z = 5$ curve in Fig. 3 – are specific to the dependence of $z_{1/2}$ on $M_{\rm d,vir}(0)$ in our equation (25). That and equation (26) only give an *approximation* to the numerical results of van den Bosch et al. (2014) for the *median* most massive progenitors of haloes with 10^{11} M$_\odot \lesssim M_{\rm d,vir}(0) \lesssim 10^{15}$ M$_\odot$. Fine details following from them are not definitive, especially at the highest end of the $z = 0$ mass range. However, the flattening of $M_{\rm d,vir}(z)$ as a function of $M_{\rm d,vir}(0)$ is qualitatively robust. It ultimately has some implications for the shape of the black hole M–σ relation at high σ-values, which we discuss further in Section 4.

In the bottom panel of Fig. 3, at any fixed redshift the different halo models give greater differences in $V_{\rm d,pk}(z)/V_{\rm d,pk}(0)$ for lower virial masses. This is because lower mass haloes generally have higher concentrations $r_{\rm vir}/r_{-2}$, and therefore higher ratios of $r_{\rm vir}/r_{\rm pk}$ (see equation 24). Thus, the ratio $V_{\rm d,pk}/V_{\rm d,vir}$ is more sensitive in lower mass haloes to the model-dependent steepness of the circular-speed curve at radii $r > r_{\rm pk}$. But $V^2_{\rm d,vir} \propto M_{\rm d,vir}(z)/r_{\rm vir}(z)$ is independent of the halo density profile, and so only $V_{\rm d,pk}$ is actually model-dependent. Since NFW and Burkert (1995) haloes have circular-speed curves that are intermediate in steepness to Dehnen & McLaughlin and Hernquist models beyond $r_{\rm pk}$ (see Fig. 2), the curves for $V_{\rm d,pk}(z)/V_{\rm d,pk}(0)$ versus $M_{\rm d,vir}(0)$ in these other models lie between the two shown in Fig. 3.

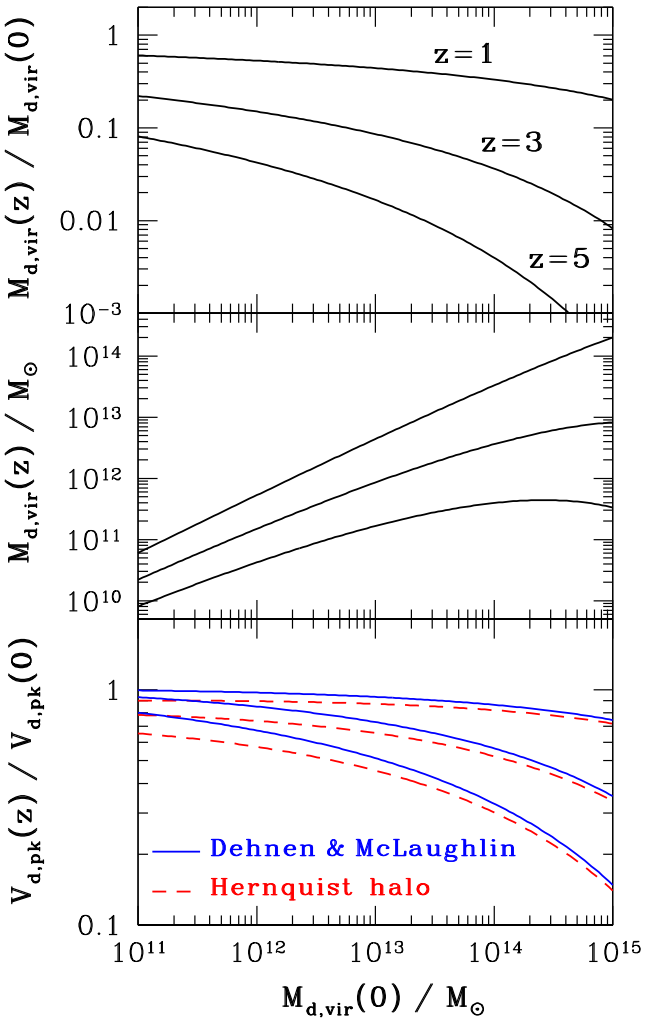

Figure 3. Top panel: relative virial masses $M_{\rm d,vir}(z)/M_{\rm dvir}(0)$ for the most massive progenitors of haloes with masses $M_{\rm d,vir}(0)$ at $z = 0$, as given by equations (25) and (26). From top to bottom, the curves are for the progenitors at fixed redshifts $z = 1$, 3 and 5. Middle panel: virial masses of the most massive progenitor haloes at $z = 1, 3$ and 5 (for the curves from top to bottom) plotted directly against the $z = 0$ halo mass. Bottom panel: peak circular speeds $V_{\rm d,pk}(z)$ in the most massive progenitors at $z = 1, 3$ and 5, relative to the peak speeds $V_{\rm d,pk}(0)$ in the final haloes at $z = 0$, from equation (28). The solid (blue) lines are for haloes with a Dehnen & McLaughlin (2005) density profile and the dashed (red) lines are for haloes with a Hernquist (1990) profile. These bracket the corresponding curves for NFW and Burkert (1995) haloes at the same redshifts.

3 GALAXY AND HALO SCALINGS AT $z = 0$

A two-component model for a spherical galaxy is formally defined by four parameters: $R_{\rm e}$ and $M_{*,\rm tot}$ for the stars, which we assume here to follow Hernquist (1990) density profiles (summarized in Section 2.1), plus r_{-2} and $M_{\rm d}(r_{-2})$ for a dark-matter profile (described in Section 2.2). However, there are interdependences between these parameters: $R_{\rm e}$ and $M_{*,\rm tot}$ are correlated (discussed just below), while the radii and masses of dark-matter haloes are connected to each other and to $M_{*,\rm tot}$ by cosmological simulations (the stellar mass fractions in Section 2.3 and the concentrations in Section 2.5). These dependences allow the models to be put in terms of a single independent parameter, which we choose to be $M_{*,\rm tot}$.

Fig. 4 shows the average trends for various galaxy properties versus $M_{*,\rm tot}$ at $z = 0$, together in some cases with data from the literature. In this section, we detail the procedures leading to these plots. In Section 4, we fold in the redshift evolution of $V_{\rm d,pk}$ (from Section 2.6) to apply equation (1) for predicted black hole masses and consider the empirical correlation between $M_{\rm BH}$ and the stellar $\sigma_{\rm ap}(R_{\rm e})$.

Our goal here is to establish representative trend-line relationships between various stellar and halo properties. Scatter around the trends is inevitable, and it can contain physical information, but in this paper we set aside the task of characterizing or explaining any scatter in detail.

3.1 Stellar masses and effective radii

Panel (a) of Fig. 4 plots effective radius against total stellar mass for local early-type galaxies in two data sets: 258 systems from the ATLAS$^{\rm 3D}$ survey (squares; Cappellari et al. 2011, 2013a,b) and 100 from the ACS Virgo Cluster Survey (ACSVCS, triangles; Côté et al. 2004; Chen et al. 2010).

In each case, the effective radii are tabulated by the original authors, either in kpc directly or as angular sizes along with the distances to individual galaxies. To estimate the stellar masses, we have taken integrated luminosities provided by the authors and calculated mass-to-light ratios using the single-burst population-synthesis models of Maraston (1998, 2005) assuming stellar ages of 9 Gyr and a Kroupa (2001) stellar initial mass function (IMF). The masses in these M/L ratios include both luminous stars and dark remnants. We have also used Bruzual & Charlot (2003) models to confirm that extended star formation lasting as long as 6 Gyr gives the same M/L values, to within $\lesssim 5$ per cent, when the mean stellar age is 9 Gyr.

Cappellari et al. (2011) give K-band absolute magnitudes for galaxies in the ATLAS$^{\rm 3D}$ survey. At an age of 9 Gyr and for metallicities $-1.7 \le [Z/{\rm H}] \le +0.3$, the mass-to-light ratios tabulated by Maraston (2005) are $0.93 \gtrsim M_*/L_K \gtrsim 0.82\,{\rm M}_\odot\ {\rm L}_\odot^{-1}$. We therefore adopt a constant $M_*/L_K \equiv 0.88\,{\rm M}_\odot\ {\rm L}_\odot^{-1}$ for all of the ATLAS$^{\rm 3D}$ galaxies. This value changes by approximately ± 15 per cent if the mean age of the stars is changed by ± 2 Gyr.

Chen et al. (2010) give g-band apparent magnitudes and $(g - z)$ colours for the ACSVCS galaxies. Combining these with surface-brightness fluctuation distances from Blakeslee et al. (2009) allows us to calculate absolute z-band magnitudes. Then, for metallicities $-1.7 \le [Z/{\rm H}] \le +0.3$, a Kroupa IMF and an age of 9 Gyr, the Maraston models give $1.40 \lesssim M_*/L_z \lesssim 2.0\,{\rm M}_\odot\ {\rm L}_\odot^{-1}$. We have used a single $M_*/L_z \simeq 1.7\,{\rm M}_\odot\ {\rm L}_\odot^{-1}$ for all of the ACSVCS galaxies to plot the points in panel (a) of Fig. 4. Again, this changes by ± 15 per cent–20 per cent if the assumed age is changed by ± 2 Gyr.

The line going through the $R_{\rm e}$ versus $M_{*,\rm tot}$ data in Fig. 4 is a parametrization of the average correlation,

$$\frac{R_{\rm e}}{\rm kpc} = 1.5 \left(\frac{M_{*,\rm tot}}{2\times 10^{10}\,{\rm M}_\odot}\right)^{0.1} \left[1 + \left(\frac{M_{*,\rm tot}}{2\times 10^{10}\,{\rm M}_\odot}\right)^{5}\right]^{0.1}, \quad (29)$$

which we decided by eye. Roughly equal numbers of ATLAS$^{\rm 3D}$ + ACSVCS data points lie above and below this line. A ± 20 per cent change in adopted mass-to-light ratios (whether due to a different assumed mean age or a different star formation history) results in a ± 20 per cent change to the mass scale in equation (29).

The ATLAS$^{\rm 3D}$ sample covers the full range of stellar masses, $10^{10}\ {\rm M}_\odot \lesssim M_{*,\rm tot} \lesssim 10^{12}\ {\rm M}_\odot$, of the local galaxies that define the black hole M–σ relation. As mentioned in Section 2.1, the light profiles in this mass range can generally be fitted by Sérsic (1968) models with indices $n \approx$ 3–7, all of which can be

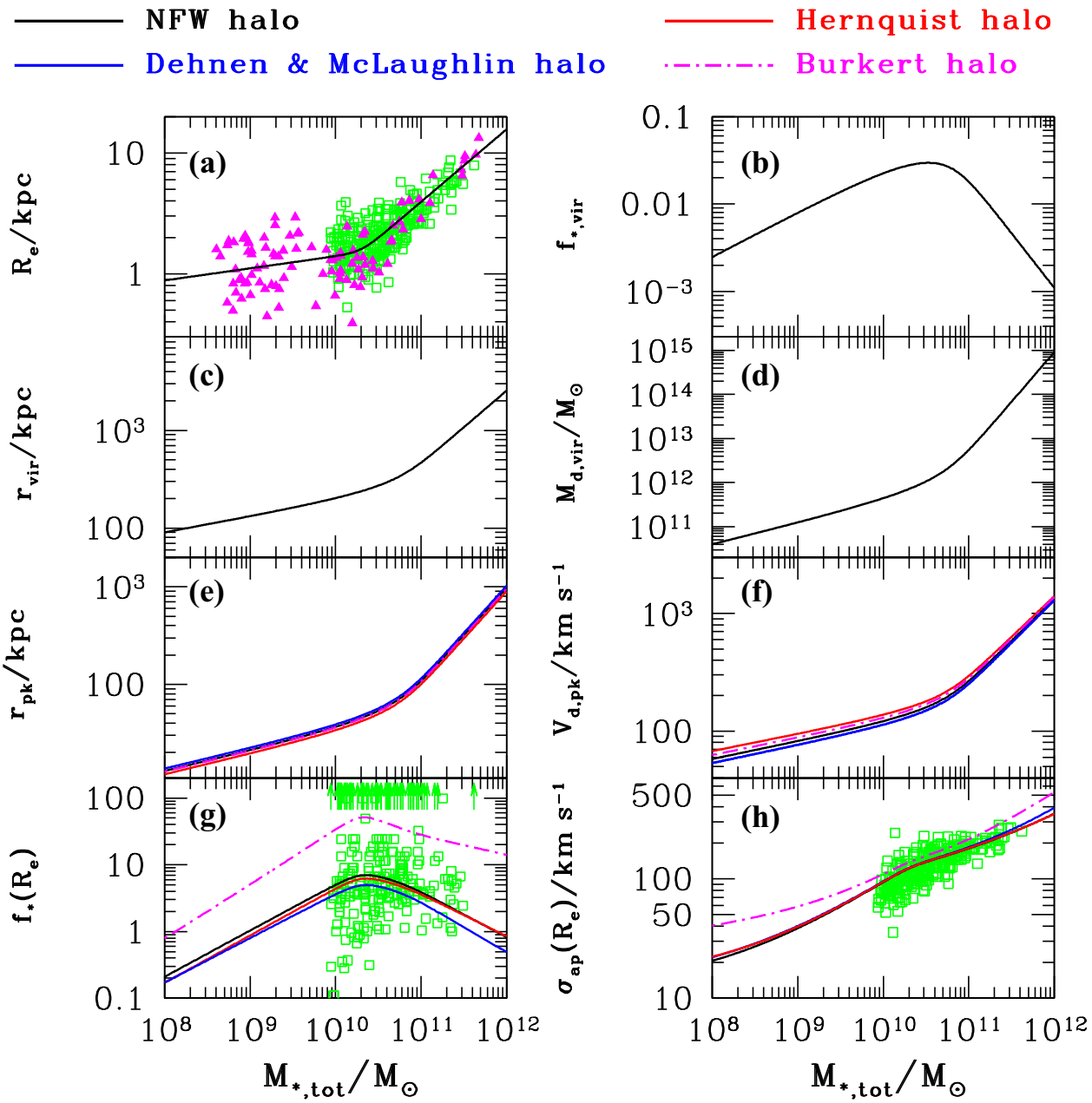

Figure 4. Model scaling relations for stellar and dark-matter halo properties versus total stellar mass, $M_{*,\rm tot}$, in spherical galaxies at $z = 0$. With the exception of the curve in panel (a), the low-mass extensions of these models to $M_{*,\rm tot} \lesssim 5 \times 10^9$ M$_\odot$ (stellar velocity dispersions $\sigma_{\rm ap}(R_{\rm e}) \lesssim 60\,{\rm km\,s^{-1}}$) should be viewed with some caution, as discussed in Section 3.6. Panel (a): stellar effective radius, $R_{\rm e}$. Data points represent galaxies in the ATLAS$^{\rm 3D}$ survey (Cappellari et al. 2011, green squares) and the ACS Virgo Cluster Survey (Chen et al. 2010, magenta triangles). See Section 3.1 for details. Panel (b): ratio $f_{*,\rm vir}$ of stellar to dark-matter mass within the virial radius; see Sections 2.3 and 3.2. Panel (c): virial radius, $r_{\rm vir}$; see Section 3.2. Panel (d): mass of dark matter within the virial radius, $M_{\rm d,vir}$; see Section 3.2. Panel (e): radius $r_{\rm pk}$ where the dark-matter circular-speed curve peaks. The different coloured curves are for four different models of the dark-matter density profile. See Sections 2.2 and 3.3 for details. Panel (f): peak value of the dark-matter circular speed, $V_{\rm d,pk}$, assuming each of the four different dark-matter halo models; see Section 3.3. Panel (g): ratio $f_*(R_{\rm e})$ of stellar mass to dark-matter mass within a sphere of radius $r < R_{\rm e}$, for each of the four different halo models; see Section 3.4. Data points are from dynamical modelling by the ATLAS$^{\rm 3D}$ survey (Cappellari et al. 2013a,b); arrows at the top of the panel represent galaxies consistent in their analysis with having no dark matter inside $R_{\rm e}$. Panel (h): stellar velocity dispersion $\sigma_{\rm ap}(R_{\rm e})$ within an aperture of radius $R_{\rm e}$. Data points are taken from the ATLAS$^{\rm 3D}$ survey. See Section 3.5 for details.

approximated adequately, for our purposes, by a Hernquist (1990) profile in projection. The ACSVCS galaxies include many with $M_{*,\rm tot} < 10^{10}\,{\rm M}_\odot$, where surface-brightness profiles are increasingly better fitted by lower index Sérsic functions tending towards exponentials. We have included these systems mainly to ensure that our analysis incorporates the change in slope that they show in the $R_{\rm e}$–$M_{*,\rm tot}$ correlation. In all of what follows, we address with some care the extent to which our results might (or may not) be put in error by assuming Hernquist stellar-density profiles for all systems.

3.2 Virial radii and halo virial masses

For any value of $M_{*,\rm tot}$, equation (29) gives a typical value for $R_{\rm e}$. Assuming a Hernquist density profile for the stars, we can then write, for the ratio of stellar to dark-matter mass within the virial radius of a galaxy,

$$f_{*,\rm vir} \equiv \frac{M_*(r_{\rm vir})}{M_{\rm d}(r_{\rm vir})} = \frac{M_{*,\rm tot}}{M_{\rm d,vir}}\left[\frac{r_{\rm vir}/R_{\rm e}}{r_{\rm vir}/R_{\rm e}+1/\mathscr{R}}\right]^2 \tag{30}$$

with $\mathscr{R} \simeq 1.815\,27$ (see equation 3). Understanding the dark-matter mass to be that of the main halo *centred* on the stars in the galaxy, $f_{*,\rm vir}$ is additionally constrained by cosmological simulations, as discussed in Section 2.3 and represented by equation (20) above from Moster et al. (2010). Repeating this for convenience, at $z = 0$ we have

$$f_{*,\rm vir} = 0.0564\left\{\left[\frac{M_{\rm d,vir}}{7.66\times10^{11}\,{\rm M}_\odot}\right]^{-1.06} + \left[\frac{M_{\rm d,vir}}{7.66\times10^{11}\,{\rm M}_\odot}\right]^{+0.556}\right\}^{-1}. \tag{31}$$

Finally, if the total mass within $r_{\rm vir}$ is simply the sum of the dark matter plus the stars in the central galaxy, i.e. $M(r_{\rm vir}) = M_{\rm d,vir}(1 + f_{*,\rm vir}t)$, then the definition of $r_{\rm vir}$ in equation (23) gives (at $z = 0$ for the 2013 *Planck* cosmological parameters)

$$f_{*,\rm vir} = 0.0544\left[\frac{r_{\rm vir}}{100{\rm kpc}}\right]^3\left[\frac{M_{\rm d,vir}}{10^{12}\,{\rm M}_\odot}\right]^{-1} - 1. \tag{32}$$

Solving equations (30)–(32) for all of $f_{*,\rm vir}$, $r_{\rm vir}$ and $M_{\rm d,vir}$ as functions of $M_{*,\rm tot}$ gives the curves shown in panels (b), (c) and (d) of Fig. 4. These are independent of any assumptions about the internal density profiles of the haloes.

The peak in $f_{*,\rm vir}$ in panel (b), at a value of $\simeq 0.03$ for $M_{*,\rm tot} \simeq 3.4\times10^{10}\,{\rm M}_\odot$ or $M_{\rm d,vir} \simeq 1.1\times10^{12}\,{\rm M}_\odot$, comes directly from the form of equation (31) taken from Moster et al. (2010). It is intriguing that the mass scale of this peak is close to the mass where the empirical $R_{\rm e}$–$M_{*,\rm tot}$ correlation changes slope (equation 29), but we do not pursue this issue here. The immediate point is that $f_{*,\rm vir}$ decreases rapidly towards higher masses, such that the haloes around central galaxies with $M_{*,\rm tot} \gtrsim 10^{11}\,{\rm M}_\odot$ have $M_{\rm d,vir} \gtrsim 10^{13}\,{\rm M}_\odot$ and $r_{\rm vir} \gtrsim 500\,{\rm kpc}$. They encompass entire groups and clusters.

For the massive systems in particular, there may be baryons that reside in the halos but are not associated directly with the stars of the central galaxy – intracluster light and gas, and the stars in any off-centre satellite galaxies. Equation (32) for the virial radius takes no account of any such 'extra' baryons. To do so properly would require additionally constraining the global baryon fraction in galaxy clusters, which is itself a mass-dependent quantity (see, e.g., Giodini et al. 2009; McGaugh et al. 2010; Zhang et al. 2011). However, in no case would the total virial mass be increased by more than $\simeq 15$ per cent (this being the cosmic average baryon fraction, $\Omega_{b,0}/\Omega_{m,0}$), and hence the virial radius would not increase by more than $\simeq 5$ per cent. We therefore ignore the complication as far as $r_{\rm vir}$ is concerned.

Then, over the range of galaxy masses shown in Fig. 4, we find that $110 \lesssim r_{\rm vir}/R_{\rm e} \lesssim 170$. As a result, the stellar mass inside the virial radius is $M_*(r_{\rm vir}) \gtrsim 0.99\,M_{*,\rm tot}$ in all cases, and equation (30) says that $f_{*,\rm vir} \simeq M_{*,\rm tot}/M_{\rm d,vir}$ with only a very weak dependence on $r_{\rm vir}/R_{\rm e}$. The mass of dark matter *alone* within $r_{\rm vir}$ is then determined [through equation (31)] by $M_{*,\rm tot}$ almost independently of $r_{\rm vir}$. Thus, our values for $M_{\rm d,vir}$ would not be changed discernibly by having additional baryons distributed in the haloes outside of the central galaxies.

These conclusions still hold if the stars in the central galaxies are described by Sérsic models that depart significantly from Hernquist profiles in projection, so long as $M_*(r)$ still essentially converges within $r \lesssim 100\,R_{\rm e}$. Hence, the curves for $f_{*,\rm vir}$, $r_{\rm vir}$ and $M_{\rm d,vir}$ versus $M_{*,\rm tot}$ in Fig. 4 are insensitive to the choice of stellar density profile.

3.3 Peak halo circular speeds

With virial radii and dark-matter virial masses known as functions of $M_{*,\rm tot}$, the scale r_{-2} follows from equation (24) in Section 2.5 for the concentration $r_{\rm vir}/r_{-2}$ versus $M_{\rm d,vir}$ (Dutton & Macciò 2014), evaluated at $z = 0$. The location of the peak of the dark-matter circular-speed curve then comes from the ratio $r_{\rm pk}/r_{-2}$ specific to a choice of $\rho_{\rm d}(r)$ for the dark matter [one of equations (7), (11), (15) or (19) in Section 2.2]. Panel (e) of Fig. 4 shows the final curves of $r_{\rm pk}$ versus $M_{*,\rm tot}$ for all four of the halo profiles we are considering. There is little difference between the curves because we have assumed the same $(r_{\rm vir}/r_{-2})$ versus $M_{\rm d,vir}$ relation for all halo models, and because $r_{\rm pk}/r_{-2} = 2$–2.3 for all of them. They are also essentially independent of the form of the stellar density profile, because the underlying curves of $r_{\rm vir}$ and $M_{\rm d,vir}$ versus $M_{*,\rm tot}$ are. Ultimately, we have approximately $15 \lesssim r_{\rm pk}/R_{\rm e} \lesssim 70$ and $0.14 \lesssim r_{\rm pk}/r_{\rm vir} \lesssim 0.40$ for stellar masses in the range $10^8\,{\rm M}_\odot \lesssim M_{*,\rm tot} \lesssim 10^{12}\,{\rm M}_\odot$.

The peak value of the dark-matter circular speed is obtained as

$$V^2_{\rm d,pk} = \frac{V^2_{\rm d}(r_{\rm pk})/V^2_{\rm d}(r_{-2})}{V^2_{\rm d}(r_{\rm vir})/V^2_{\rm d}(r_{-2})}\frac{G\,M_{\rm d,vir}}{r_{\rm vir}}. \tag{33}$$

The normalized circular-speed profiles $V^2_{\rm d}(r)/V^2_{\rm d}(r_{-2})$ for different halo models are shown in Fig. 2 and given in equations (6), (10), (14) and (18) of Section 2.2. Evaluating the appropriate one of these at $r_{\rm pk}/r_{-2}$ and $r_{\rm vir}/r_{-2}$ after choosing a density profile $\rho_{\rm d}(r)$, and then folding in the dependences of $M_{\rm d,vir}$ and $r_{\rm vir}$ on $M_{*,\rm tot}$, yields $V_{\rm d,pk}$ at any given total stellar mass. The results are shown in panel (f) of Fig. 4.

The curves for $V_{\rm d,pk}$ versus $M_{*,\rm tot}$ are again insensitive to the use of a Hernquist profile for the stellar distributions. The differences between them come from the (small) differences in the values of $r_{\rm pk}/r_{-2}$ in the different halo models, and the (larger) differences in the widths of the normalized circular-speed curves between $r_{\rm pk}$ and $r_{\rm vir}$, as seen in Fig. 2. The differences are greater for systems with smaller $M_{*,\rm tot}$ because those haloes are less massive and have higher concentrations on average, with larger ratios $r_{\rm vir}/r_{\rm pk}$ and hence ratios $V_{\rm d}(r_{\rm pk})/V_{\rm d}(r_{\rm vir})$ that are more sensitive to the shape of the circular-speed curve at large radii in a halo.

It is clear that the circular speeds $V_{\rm d,pk}$ for the most massive model galaxies, which represent those defining the upper end of the observed black hole M–σ relation, will far exceed the stellar velocity dispersions measured within $R_{\rm e}$ in the real systems. This is because the dark-matter haloes centred on such massive galaxies correspond to entire clusters. It is also why the naive substitution $V_{\rm d,pk} = \sqrt{2}\,\sigma_{\rm ap}(R_{\rm e})$, inspired by the singular isothermal sphere, cannot suffice for a proper comparison of a prediction like equation (1) to the M–σ data (cf. Fig. 1). At the same time, the most massive haloes are the ones that will have grown the most at low redshifts, *after* the epoch of peak quasar activity that may have mainly determined self-regulated black hole masses. Hence, it is essential that $V_{\rm d,pk}$ be calculated in the *progenitors* of haloes if equation (1) is to be assessed self-consistently.

3.4 Stellar mass fractions inside R_e

The ratio of stellar mass to dark-matter mass contained within radius r in a galaxy with a specified total stellar mass can be written as

$$f_*(r) \equiv \frac{M_*(r)}{M_d(r)} = f_{*,\rm vir}\,\frac{M_*(r)/M_*(r_{\rm vir})}{M_d(r)/M_d(r_{\rm vir})}. \quad (34)$$

Here, $f_{*,\rm vir}$ is known from above as a function of $M_{*,\rm tot}$. The normalized stellar mass profile $M_*(r)/M_*(r_{\rm vir})$ comes from equation (3) for a Hernquist density profile and is determined by $M_{*,\rm tot}$ because R_e and $r_{\rm vir}$ are. Once a dark-matter halo model has been chosen, the mass profile $M_d(r)/M_d(r_{\rm vir})$ follows from one of equations (5), (9), (13) or (17) and is also determined by $M_{*,\rm tot}$ because that fixes the concentration $r_{\rm vir}/r_{-2}$.

The function $f_*(r)$ enters into the Jeans equation for calculations of the stellar velocity dispersion in Section 3.5. First, however, we evaluate it specifically at the radius $r = R_e$ for galaxies with a range of stellar masses, in order to compare our results with some additional data.

Cappellari et al. (2013a,b) have used dynamical (Jeans) modelling to estimate the ratio of dark to total mass within a *sphere* of radius $r = R_e$ for each of the ATLAS^{3D} galaxies. This fraction, which they denote $f_{\rm dm}$, is related to our stellar-to-dark mass ratio within $r < R_e$ by $f_*(R_e) = f_{\rm dm}^{-1} - 1$. Although the Cappellari et al. modelling assumes that dark-matter haloes have NFW density profiles, their results are not sensitive to this detail, since usually $M_d(R_e) < M_*(R_e)$ by factors of several in their galaxies – see Cappellari et al. (2013a) for further details.

Panel (g) of Fig. 4 shows the $f_*(R_e)$ data for 258 ATLAS^{3D} galaxies (arrows at the top of the panel indicate galaxies for which the modelling by Cappellari et al. is consistent with no dark matter inside $r < R_e$). The curves show the typical $f_*(R_e)$ expected at a given $M_{*,\rm tot}$ on the basis of our equation (34), for each of the four different dark-matter halo profiles.

These curves depend on the stellar density profile as $f_*(R_e) \propto M_*(R_e)/M_*(r_{\rm vir}) \simeq M_*(R_e)/M_{*,\rm tot}$. In the mass range $M_{*,\rm tot} \gtrsim 10^{10}$ M$_\odot$, describing the stars by Sérsic models with $3 \lesssim n \lesssim 7$ rather than by Hernquist models alters $M_*(R_e)/M_{*,\rm tot}$, and hence $f_*(R_e)$, by less than 5 per cent. Much lower mass galaxies, which have no $f_*(R_e)$ data in Fig. 4 and are not represented in the empirical M–σ relation, will have closer to exponential surface-brightness profiles. For these, $M_*(R_e)/M_{*,\rm tot}$ and $f_*(R_e)$ are lower than the Hernquist model values, but by no more than $\simeq 20$ per cent.

The curves are rather more sensitive to the choice of dark-matter halo profile, in particular to how steeply the enclosed mass $M_d(r)$ decreases inwards to $r \to 0$. This is reflected in the shapes of the circular-speed curves in Fig. 2. For a given value of $M_{*,\rm tot}$, and hence $M_d(r_{\rm vir})$, NFW and Hernquist haloes have similar values for $M_d(R_e)/M_d(r_{\rm vir})$, and thus for $f_*(R_e)$, because of their identical central structures. Dehnen & McLaughlin (2005) haloes have higher $M_d(R_e)/M_d(r_{\rm vir})$ and lower $f_*(R_e)$ for the same stellar mass, because they have significantly shallower mass profiles than either NFW or Hernquist haloes. The much steeper $M_d(r)$ or $V_d^2(r)$ profiles in the constant-density cores of Burkert (1995) models put substantially more dark matter at large radii in these haloes, giving lower values of $M_d(R_e)/M_d(r_{\rm vir})$ and higher $f_*(R_e)$ for a fixed $M_{*,\rm tot}$.

The three dark-matter haloes with central density cusps all imply $f_*(R_e)$ values that are broadly consistent with the data in Fig. 4(g) for systems with $M_{*,\rm tot} \gtrsim 10^{10}$ M$_\odot$. However, the cored halo of Burkert (1995) is incompatible with these data. This is a valuable check on our calculations, and an argument for not considering Burkert haloes further in the context of the black hole M–σ relation for intermediate- and high-mass galaxies. But it is not surprising, since the Burkert model was originally proposed only in connection with dwarf spheroidal galaxies, not regular ellipticals.

3.5 Stellar velocity dispersions

To calculate stellar velocity dispersions, we solve the isotropic Jeans equation including contributions to the gravitational potential from the dark matter, the stars *and* the accumulated ejecta from stellar winds and supernovae over the lifetime of a galaxy. Assuming that these ejecta are confined to the central regions of the overall potential well in relatively large galaxies, we approximate their mass profile as $M_{\rm ej}(r) \approx F_{\rm ej} M_*(r)$ with $F_{\rm ej}$ a constant. The value of $F_{\rm ej}$ comes from the same single-burst population-synthesis models that we used in Section 3.1 to calculate stellar mass-to-light ratios. Namely, for a Kroupa (2001) stellar IMF and stellar ages greater than several Gyr, Maraston (2005) gives the ratio of current to initial mass in stars (and remnants) as $\simeq 0.58$. Thus, in our notation, $(1 + F_{\rm ej}) \simeq 1/0.58$. The value of $F_{\rm ej}$ is robust to any changes in the star formation history, with a <2 per cent increase for extended star formation.

With dimensionless radii, stellar densities and one-dimensional velocity dispersions defined as

$$\widetilde{r} \equiv \frac{r}{R_e}; \qquad \widetilde{\rho}_* \equiv \frac{\rho_*}{M_{*,\rm tot}/R_e^3}; \qquad \widetilde{\sigma}_*^2 \equiv \frac{\sigma_*^2}{GM_{*,\rm tot}/R_e},$$

the isotropic and spherical Jeans equation is

$$\frac{\mathrm{d}}{\mathrm{d}\widetilde{r}}[\widetilde{\rho}_*(\widetilde{r})\widetilde{\sigma}_*^2(\widetilde{r})] = -\frac{\widetilde{\rho}_*(\widetilde{r})}{\widetilde{r}^2}\,\frac{M_*(\widetilde{r})}{M_{*,\rm tot}}\left[(1+F_{\rm ej}) + \frac{1}{f_*(\widetilde{r})}\right]. \quad (35)$$

The profiles $\widetilde{\rho}_*(\widetilde{r})$ and $M_*(\widetilde{r})/M_{*,\rm tot}$ are given by equations (2) and (3) in Section 2.1 for a Hernquist model, while $(1 + F_{\rm ej}) = 1/0.58$ as just mentioned. The function $f_*(\widetilde{r}) \equiv M_*(\widetilde{r})/M_d(\widetilde{r})$ is known in full for any specific value of $M_{*,\rm tot}$ (and choice of dark-matter density profile) as discussed in Section 3.4. Subject to the boundary condition that $\widetilde{\rho}_*\,\widetilde{\sigma}_*^2 \to 0$ as $\widetilde{r} \to \infty$, equation (35) can therefore be solved for the dimensionless $\sigma_*^2/\left(GM_{*,\rm tot}/R_e\right)$ as a function of r/R_e in a galaxy with any given total stellar mass.

The aperture velocity dispersion over a circular disc on the plane of the sky comes from projecting $\sigma_*^2(r)$ along the line of sight and then taking a luminosity-weighted average. Defining the dimensionless projected radius $\widetilde{R} \equiv R/R_e$, the stellar surface density profile is first obtained as

$$\widetilde{\Sigma}_*(\widetilde{R}) \equiv \frac{\Sigma_*(R)}{M_{*,\rm tot}/R_e^2} = 2\int_{\widetilde{R}}^{\infty} \widetilde{\rho}_*(\widetilde{r})\,\frac{\widetilde{r}\,\mathrm{d}\widetilde{r}}{(\widetilde{r}^2 - \widetilde{R}^2)^{1/2}}; \quad (36)$$

then the projected stellar velocity dispersion profile is

$$\widetilde{\sigma}_{\rm p}^2(\widetilde{R}) = \frac{2}{\widetilde{\Sigma}_*(\widetilde{R})}\int_{\widetilde{R}}^{\infty} \widetilde{\rho}_*(\widetilde{r})\widetilde{\sigma}_*^2(\widetilde{r})\,\frac{\widetilde{r}\,\mathrm{d}\widetilde{r}}{(\widetilde{r}^2 - \widetilde{R}^2)^{1/2}}; \quad (37)$$

and the aperture dispersion within projected radius $R_{\rm ap}$ is

$$\frac{\sigma_{\rm ap}^2(R_{\rm ap})}{GM_{*,\rm tot}/R_e} = \left[\int_0^{R_{\rm ap}/R_e} \widetilde{\sigma}_{\rm p}^2(\widetilde{R})\widetilde{\Sigma}_*(\widetilde{R})\widetilde{R}\,\mathrm{d}\widetilde{R}\right] \times \left[\int_0^{R_{\rm ap}/R_e} \widetilde{\Sigma}_*(\widetilde{R})\widetilde{R}\,\mathrm{d}\widetilde{R}\right]^{-1}. \quad (38)$$

The right-hand side of this is determined entirely by $M_{*,\rm tot}$ once a halo model has been chosen and a value of $R_{\rm ap}$ specified. Setting $R_{\rm ap} = R_e$ yields the model $\sigma_{\rm ap}$ that corresponds to the measured velocity dispersions in the McConnell & Ma (2013) compilation of SMBH M–σ data.

Panel (h) of Fig. 4 shows the calculated $\sigma_{\rm ap}(R_{\rm e})$ versus $M_{*,\rm tot}$ for each of the four different dark-matter halo models. The points are data for the ATLAS$^{\rm 3D}$ galaxies, taken again from Cappellari et al. (2011, 2013a,b, the ACSVCS galaxies included in the plot of $R_{\rm e}$ versus $M_{*,\rm tot}$ do not have published velocity dispersions). All of the cuspy haloes give curves that run through the middle of the $\sigma_{\rm ap}(R_{\rm e})$ data, while the cored Burkert (1995) halo predicts velocity dispersions that are higher for a given $M_{*,\rm tot}$. A Burkert halo has relatively more of its mass at larger radii than the cuspy haloes do. The unprojected $\sigma_*(r)$ is substantially higher around and beyond $r \sim R_{\rm e}$ as a result, which inflates the line-of-sight dispersion even inside $R_{\rm e}$ and boosts the aperture dispersion noticeably.

The dimensionless aperture dispersion inside $R_{\rm e}$ for a self-consistent Hernquist sphere of stars only, with no ejecta or dark matter ($F_{\rm ej} = 0$ and $1/f_*(r) \equiv 0$), is $\sigma_{\rm ap}(R_{\rm e})/\left(GM_{*,\rm tot}/R_{\rm e}\right)^{1/2} \simeq 0.389$. Based on this, the dispersion with ejecta and dark matter included can be usefully approximated by the function

$$\frac{\sigma_{\rm ap}(R_{\rm e})}{\sqrt{GM_{*,\rm tot}/R_{\rm e}}} \approx 0.389 \sqrt{\left(1+F_{\rm ej}\right) + \frac{0.86}{f_*(R_{\rm e})}}\,, \tag{39}$$

where the term under the square root represents the ratio of an 'effective' total mass to the total stellar mass. This formula reproduces the values from our full calculations with relative error <2.5 per cent for any $f_*(R_{\rm e}) > 0.1$ in any of an NFW, Hernquist or Dehnen & McLaughlin halo.

We have also calculated $\sigma_{\rm ap}(R_{\rm e})/(GM_{*,\rm tot}/R_{\rm e})^{1/2}$ for self-gravitating Sérsic (1968) $R^{1/n}$ spheres without any dark matter. For indices $n \lesssim 5$ – which apply to giant ellipticals and dwarfs with masses down to $M_{*,\rm tot} \sim 10^8$–$10^9\,{\rm M}_\odot$ – we find $0.36 \lesssim \tilde{\sigma}_{\rm ap}(R_{\rm e}) \lesssim 0.43$, as compared to $\tilde{\sigma}_{\rm ap}(R_{\rm e}) \simeq 0.389$ for the Hernquist model. Thus, over most of the mass range in Fig. 4, the model curves for $\sigma_{\rm ap}(R_{\rm e})$ are vulnerable at only the $\lesssim 10$ per cent level to bias (a slight tilt) resulting from our use of a Hernquist profile to describe all of the stellar distributions. Very massive ellipticals with $M_{*,\rm tot} \gtrsim 2$–$3 \times 10^{11}\,{\rm M}_\odot$ are generally fitted by Sérsic indices $n \approx 5$–7, for which $\sigma_{\rm ap}(R_{\rm e})/(GM_{*,\rm tot}/R_{\rm e})^{1/2} \simeq 0.43$–$0.49$ rather than 0.389. However, a small compensation in our parametrization of $R_{\rm e}$ versus $M_{*,\rm tot}$ at high masses then suffices to yield essentially the same $\sigma_{\rm ap}(R_{\rm e})$ as the curve in Fig. 4(h).

3.6 Discussion

3.6.1 *Dwarf galaxies*

There are more physical considerations than the validity of a Hernquist profile for the stellar distribution, which affect how well our models might be able to describe galaxies with stellar masses less than a few $\times 10^9\,{\rm M}_\odot$.

In order to calculate velocity dispersions in Section 3.5, we assumed that stellar ejecta are retained at the bottom of any galaxy's potential well. However, supernova-driven winds will have expelled the ejecta from many dwarf ellipticals to far beyond the stellar distributions. In this case, $F_{\rm ej} = 0$ in equations (35) and (39) is more appropriate than $(1 + F_{\rm ej}) = 1/0.58$. This lowers the expected $\sigma_{\rm ap}(R_{\rm e})$ by ≈ 30 per cent at a given $M_{*,\rm tot}$ for a given halo density profile.

On the other hand, the same galactic winds may cause changes in the central structures of the dark-matter haloes of dwarfs, from initially steep density cusps to shallower profiles perhaps closer to the Burkert (1995) model (e.g. Burkert & Silk 1997; Pontzen & Governato 2012), while subsequent tidal stripping could have led to further modifications at large radii in the haloes. Substantial, systematic alterations to the dark-matter density profiles may impact the values we infer for $V_{\rm d,pk}$, $f_*(R_{\rm e})$ and $\sigma_{\rm ap}(R_{\rm e})$ from a given $M_{*,\rm tot}$, $R_{\rm e}$ and $M_{\rm d,vir}$. And in any case, the relationship connecting $M_{*,\rm tot}$ to $M_{\rm d,vir}$ in equation (20), from Moster et al. (2010), may itself be in error if extrapolated to halo masses much below $M_{\rm d,vir} \lesssim 10^{11}\,{\rm M}_\odot$ (see Behroozi et al. 2013).

All in all, while the model curves in Fig. 4 can be viewed as broadly indicative of the situation for dwarf galaxies, they should also be seen as provisional in that regime. More comprehensive modelling is required to be confident of how these kinds of average trends extrapolate to stellar masses much less than several $\times\, 10^9\,{\rm M}_\odot$ (or, roughly, $\sigma_{\rm ap}(R_{\rm e}) \lesssim 60$–$70\,{\rm km\,s^{-1}}$).

3.6.2 *Intracluster baryons*

As already discussed in Section 3.2, we can safely ignore any small differences that intracluster baryons (whether gas or stars) might make to the virial radii and masses we calculate for haloes centred on the most massive galaxies. Equation (39) in Section 3.5 now provides a way to assess the effects of intracluster baryons on the stellar velocity dispersions in the central galaxies of groups and clusters.

If additional baryonic mass is distributed spatially like the dark matter, then it can be accounted for in the Jeans equation (35), and hence in equation (39), by decreasing $f_*(r) \equiv M_*(r)/M_{\rm d}(r)$ by a constant factor. This factor will be largest if the global baryon fraction in a halo is equal to the cosmic average value but only a trace amount is actually contained in the central galaxy itself. Thus, an 'effective' $f_*(r)$ in the Jeans equation might be lower than the Moster et al. (2010) value by a factor of $(1 - \Omega_{b,0}/\Omega_{m,0})^{-1}$ at most, which is $\simeq$1.18 for a 2013 *Planck* cosmology. This could plausibly be the situation in haloes with $M_{\rm d}(r_{\rm vir}) \sim 10^{15}\,{\rm M}_\odot$ (which have $M_{*,\rm tot} \sim 10^{12}\,{\rm M}_\odot$ for the central galaxy), but the total baryon fraction decreases systematically with decreasing (sub)halo mass (e.g. McGaugh et al. 2010; Zhang et al. 2011; Gonzalez et al. 2013). In galaxy-sized haloes, it is generally consistent with the mass of stars, remnants and stellar ejecta in the galaxy proper, which we have already accounted for fully.

The maximum effect on $\sigma_{\rm ap}(R_{\rm e})$ in the central galaxy can be estimated by comparing the value of equation (39) with $(1 + F_{\rm ej}) = 1/0.58$ and $f_*(R_{\rm e}) = 0.5$ – the lowest value in any of our models at $M_{*,\rm tot} = 10^{12}\,{\rm M}_\odot$ or $M_{\rm d,vir} \simeq 10^{15}\,{\rm M}_\odot$ in Fig. 4 – to the value using $f_*(R_{\rm e}) = 0.5/1.18$ instead. The result is an increase of < 5 per cent in the velocity dispersion. This is of the same order as the maximum effect on our values for the halo virial radii. We have chosen to ignore intracluster baryons altogether rather than introduce detailed additional modelling just to make adjustments that are *at most* so small.

3.6.3 *Comparisons to individual systems*

In Appendix A, we make some checks on the average scalings represented in Fig. 4, by comparing various numbers extracted from them to relevant data in the literature for the Milky Way, M87 and M49 (the central galaxies of Virgo subclusters A and B) and NGC 4889 (the brightest galaxy in the Coma Cluster). The stellar masses and velocity dispersions of these systems span the range covered by the local early-type galaxies used to define empirical black hole M–σ relations. It is notable in particular that, starting with just the galaxies' total stellar masses, the scalings imply detailed

properties of the *cluster-sized* dark-matter haloes around each of M87, M49 and NGC 4889, which are in reasonably good agreement with literature values.

4 THE BLACK HOLE *M–σ* RELATION

The scalings in Section 3 give typical virial masses and peak circular speeds for dark-matter haloes, along with stellar velocity dispersions inside an effective radius, as one-to-one functions of galaxy stellar mass at $z = 0$. Therefore, they can be re-cast to give $M_{\rm d,vir}(0)$ and $V_{\rm d,pk}(0)$ directly as functions of the observable $\sigma_{\rm ap}(R_{\rm e})$. If a theory ties $M_{\rm BH}$ to the properties of haloes at some time in the past, then in order to predict the dependence of $M_{\rm BH}$ on $\sigma_{\rm ap}(R_{\rm e})$ (or any other galaxy properties) now, it is necessary first to connect the halo properties at $z > 0$ to those at $z = 0$.

The SMBH–halo relation we examine here is that given by equation (1) above, from McQuillin & McLaughlin (2012). To repeat,

$$M_{\rm BH} \simeq 1.14 \times 10^8 \, {\rm M}_\odot \left(\frac{f_0}{0.2}\right) \left(\frac{V_{\rm d,pk}}{200\,{\rm km\,s^{-1}}}\right)^4 . \qquad (40)$$

As discussed in Section 1.1, this equation is limited by simplifying assumptions: for example, about the nature of quasar-mode SMBH feedback (taken to be purely momentum-conserving) and the distribution of gas in protogalaxies (taken to be virialized, with ongoing cosmic infall ignored). Within these limitations it has the advantage of generality, being applicable to dark-matter haloes with any density profile.

In equation (1), $V_{\rm d,pk}$ measures the potential well of a protogalaxy that just fails to contain the quasar-mode feedback of an SMBH with mass $M_{\rm BH}$. It thus refers to conditions at a redshift marking the *end* of rapid SMBH growth by accretion at Eddington or supercritical rates in a series of gas-rich mergers. We denote this redshift by $z_{\rm qso}$. It will be different for different systems, but we expect the general range to coincide with the epoch of peak quasar number and SMBH accretion-rate densities in the Universe: namely, $z_{\rm qso} \sim 2$–4 in most cases (e.g. Richards et al. 2006; Hopkins et al. 2007a; Delvecchio et al. 2014; also Sijacki et al. 2007, 2015; Di Matteo et al. 2008).

In this Section, we apply our calculations from Section 2.6 to find *typical* values of $M_{\rm d,vir}(z_{\rm qso})$ and $V_{\rm d,pk}(z_{\rm qso})$ for the *most massive progenitors* of haloes, and hence estimate an expected $M_{\rm BH}$ in their central galaxies, as functions of the stellar $\sigma_{\rm ap}(R_{\rm e})$ at $z = 0$. This involves an assumption that the most massive progenitor halo at $z_{\rm qso} > 0$ is the one that ultimately defines the centre of the larger potential well at $z = 0$. This is statistically accurate but not always true in every individual case – see, for example, the discussion in van den Bosch et al. (2014) of the distinction between 'most massive' and 'most contributing' progenitors. Glossing over this subtlety could lead to a small amount of scatter in the SMBH *M–σ* data relative to our final curves.

The model $M_{\rm BH}$–$\sigma_{\rm ap}(R_{\rm e})$ relations we obtain do not include any growth of the SMBH itself at redshifts $z < z_{\rm qso}$, which can occur by coalescences in gas-poor galaxy mergers at the centre of a halo. However, this is distinct from the growth of the halo as a whole; many subhaloes can be accreted at low redshift that do not sink to the bottom of the potential well and thus do not grow the central SMBH. We discuss this further in Section 4.2

4.1 Halo masses and peak circular speeds at $z > 0$

The top panel of Fig. 5 shows the scaling of halo virial mass at $z = 0$ versus stellar velocity dispersion $\sigma_{\rm ap}(R_{\rm e})$ in the central galaxy at $z = 0$, obtained directly from the results of

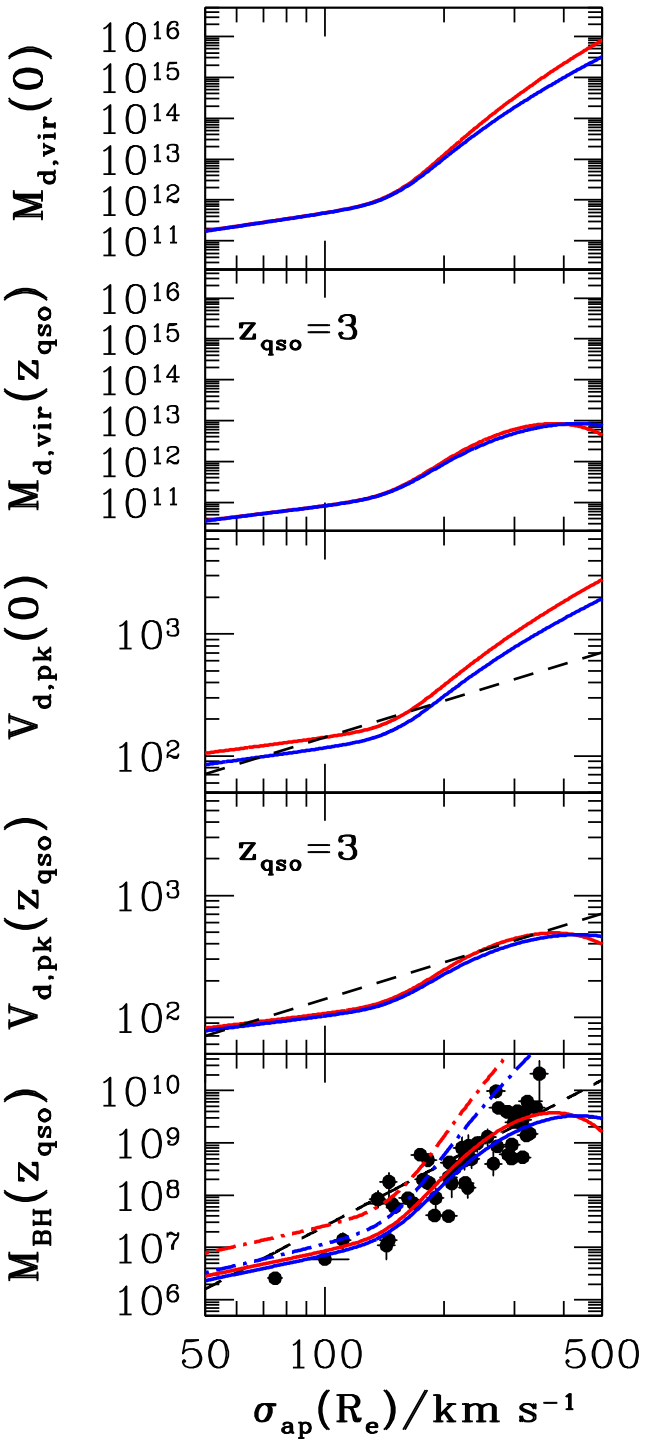

Figure 5. Top two panels: dark-matter virial mass (in $\rm M_\odot$) at $z = 0$ and at $z_{\rm qso} = 3$, versus stellar velocity dispersion $\sigma_{\rm ap}(R_{\rm e})$ at $z = 0$. Blue curves are for galaxy models with Dehnen & McLaughlin (2005) haloes; red curves have Hernquist (1990) haloes. Next two panels: peak dark-matter circular speed (in $\rm km\,s^{-1}$) at $z = 0$ and at $z_{\rm qso} = 3$, versus $\sigma_{\rm ap}(R_{\rm e})$ at $z = 0$. Blue and red curves correspond again to Dehnen & McLaughlin and Hernquist halo density profiles. The dashed straight line shows $V_{\rm d,pk} = \sqrt{2}\,\sigma_{\rm ap}(R_{\rm e})$. Bottom panel: SMBH mass (in $\rm M_\odot$) calculated from equation (1) with $f_0 = 0.18$ using the dark-matter $V_{\rm d,pk}$ at $z = 0$ (dot–dashed blue and red curves) and at $z_{\rm qso} = 3$ (solid blue and red curves), all plotted against $\sigma_{\rm ap}(R_{\rm e})$ at $z = 0$. The dashed straight line is equation (1) with $V_{\rm d,pk} \equiv \sqrt{2}\,\sigma_{\rm ap}(R_{\rm e})$. Data points are for the 53 ellipticals and lenticulars in McConnell & Ma (2013).

Section 3 [combining panels (d) and (h) of Fig. 4]. The next panel down shows $M_{\rm d,vir}$ for *the most massive progenitor of a halo* at redshift $z_{\rm qso} = 3$ [obtained from $M_{\rm d,vir}(0)$ as described in Section 2.6; see Fig. 3] against $\sigma_{\rm ap}(R_{\rm e})$ in the central galaxy at $z = 0$.

The blue curves in Fig. 5 correspond to Dehnen & McLaughlin (2005) models for the halo density profiles and the red curves to Hernquist (1990) models. These bracket the scalings obtained using NFW halo profiles, while (as discussed in Section 3) the cored halo profiles of Burkert (1995) are not appropriate in the galaxy mass range plotted here. Velocity dispersions $\sigma_{\rm ap}(R_{\rm e}) \geq 70\,{\rm km\,s^{-1}}$ at $z = 0$ correspond to stellar masses $M_{*,\rm tot} \gtrsim 8$–$9 \times 10^9\ {\rm M}_\odot$ at $z = 0$.

The next panel in the Figure shows the peak dark-matter circular speed at $z = 0$ versus stellar velocity dispersion at $z = 0$, again from Section 3 [combining panels (f) and (h) of Fig. 4]. Just below this is the scaling of $V_{\rm d,pk}$ in the most massive progenitor at $z_{\rm qso} = 3$ [obtained from $V_{\rm d,pk}(0)$ and $M_{\rm d,vir}(0)$ as in Section 2.6 and Fig. 3] versus $\sigma_{\rm ap}(R_{\rm e})$ in the central galaxy at $z = 0$. The dashed straight (black) line in these panels traces out $V_{\rm d,pk} = \sqrt{2}\,\sigma_{\rm ap}(R_{\rm e})$. This is clearly a poor substitute for the actual relationship between the two velocities at $z = 0$ in galaxies with $\sigma_{\rm ap}(R_{\rm e}) \gtrsim 200\,{\rm km\,s^{-1}}$ (or $M_{*,\rm tot} \gtrsim 3 \times 10^{11}\ {\rm M}_\odot$). It does come closer in this mass range to correctly estimating the dependence of $V_{\rm d,pk}$ at $z_{\rm qso} = 3$ on $\sigma_{\rm ap}(R_{\rm e})$ at $z = 0$; but this appears to be entirely coincidental, and the situation is reversed for $\sigma_{\rm ap}(R_{\rm e}) \lesssim 200\,{\rm km\,s^{-1}}$.

At a given value for $\sigma_{\rm ap}(R_{\rm e})$, the downward 'corrections' to $M_{\rm d,vir}$ and $V_{\rm d,pk}$, from their values at $z = 0$ to the progenitors at $z_{\rm qso} = 3$, are systematically larger for larger systems. This is a restatement of the flattening towards higher masses in the dependence of $M_{\rm d,vir}(z)$ on $M_{\rm d,vir}(0)$, which we showed in Fig. 3 and discussed there. Again, it is fundamentally because in a (Λ)CDM cosmology, more massive haloes were assembled and virialized more recently. A given range of halo mass or circular speed at $z = 0$ thus corresponds to a narrower range at any $z_{\rm qso} > 0$, and the contrast is greater for higher masses. In Fig. 5, this works to make the slopes of $M_{\rm d,vir}$ and $V_{\rm d,pk}$ versus $z = 0$ velocity dispersions significantly shallower for the halo progenitors at $z_{\rm qso} = 3$ than for the haloes themselves at $z = 0$.

The equations from Section 2.6 that underpin these results are approximations to the mass accretion histories of simulated haloes in van den Bosch et al. (2014). Those simulations extend up to halo masses $M_{\rm d,vir}(0) \lesssim 10^{15}\ {\rm M}_\odot$, corresponding to stellar $\sigma_{\rm ap}(R_{\rm e}) \lesssim$ 350–400 km s^{-1} at $z = 0$. Beyond this, our analysis is not only approximate but an extrapolation. Thus, for example, the peaks around $\sigma_{\rm ap}(R_{\rm e}) \approx 400\,{\rm km\,s^{-1}}$ in the panels of Fig. 5 for $M_{\rm d,vir}$ and $V_{\rm d,pk}$ at $z_{\rm qso} = 3$ may not be accurate. What is secure is the simple fact of the relative flatness in these curves for high stellar velocity dispersions. The same effect must appear to a greater or lesser degree for any other $z_{\rm qso} > 0$, and it directly impacts any prediction for an observable SMBH M–σ relation at $z = 0$ from a model like our equation (1) or similar.

4.2 $M_{\rm BH}$ versus $\sigma_{\rm ap}(R_{\rm e})$

The bottom panel of Fig. 5 shows SMBH mass versus $\sigma_{\rm ap}(R_{\rm e})$ at $z = 0$. The data points are for the E and S0 galaxies in the compilation of McConnell & Ma (2013). (Their data for the bulges of late-type galaxies can be seen in Fig. 1. We do not show them here because our calculations for $\sigma_{\rm ap}(R_{\rm e})$ versus $M_{*,\rm tot}$ do not allow for discs.) The dashed straight line (black), which we show purely for reference, is equation (1) evaluated with a protogalactic gas fraction of $f_0 \equiv \Omega_{b,0}/(\Omega_{m,0} - \Omega_{b,0}) = 0.18$ (for the 2013 *Planck* cosmology) and the simplistic substitution $V_{\rm d,pk} \equiv \sqrt{2}\,\sigma_{\rm ap}(R_{\rm e})$. The other curves (blue and red for Dehnen & McLaughlin and Hernquist halo density profiles) also come from equation (1) with $f_0 = 0.18$, but with $V_{\rm d,pk}$ depending on $\sigma_{\rm ap}(R_{\rm e})$ as shown in the other panels of Fig. 5.

The *broken* blue and red curves come from those for $V_{\rm d,pk}$ at $z = 0$ versus $\sigma_{\rm ap}(R_{\rm e})$ at $z = 0$ in the middle panel of Fig. 5. These are the predictions of equation (1) for the critical SMBH masses required to clear haloes filled with virialized gas in an 18 per cent mass ratio, via quasar-mode feedback *now*. It is no surprise that such predictions overshoot the M–σ data for normal early-type galaxies, quite substantially for $\sigma_{\rm ap}(R_{\rm e}) \gtrsim 200\,{\rm km\,s^{-1}}$.

The *solid* blue and red curves of $M_{\rm BH}$ versus $\sigma_{\rm ap}(R_{\rm e})$, which run through the data, are based on the curves of $V_{\rm d,pk}$ at $z_{\rm qso} = 3$ versus $\sigma_{\rm ap}(R_{\rm e})$ at $z = 0$ in the fourth panel of Fig. 5. These are predictions for the M–σ relation in quiescent galaxies at $z = 0$, if it came from an $M_{\rm BH} \propto V_{\rm d,pk}^4$ relationship established by quasar-mode feedback and blow-out from gaseous protogalaxies at $z_{\rm qso} = 3$ (with negligible subsequent SMBH growth via coalescence in mergers).

Fig. 6 gives an expanded view of $M_{\rm BH}$ versus $\sigma_{\rm ap}(R_{\rm e})$. Now, the solid (blue) curves show SMBH masses obtained from equation (1) after using our scalings to relate stellar velocity dispersion at $z = 0$ to the typical $V_{\rm d,pk}$ in progenitor haloes at a wider range of possible $z_{\rm qso} = 0, 1, 2, 3$ and 4. All of these curves assume a Dehnen & McLaughlin density profile for the dark matter; the results for NFW or Hernquist profiles are very similar. The dashed straight (black) reference line is again equation (1) with $V_{\rm d,pk} \equiv \sqrt{2}\,\sigma_{\rm ap}(R_{\rm e})$.

Most of the M–σ data at $z = 0$ lie between model curves in which an $M_{\rm BH}$–$V_{\rm d,pk}$ relation emerged from the clearing of protogalaxies by quasar-mode feedback at redshifts $2 \lesssim z_{\rm qso} \lesssim 4$. The correspondence of this range with the epoch of peak quasar activity and SMBH accretion rate in both observations and cosmological simulations is encouraging. Equation (1) represents a highly simplified, broad-brush picture of just a few processes at a critical stage of galaxy and black hole formation; but the fundamental connection it makes between protogalactic dark-matter haloes and SMBH masses appears to be along the right lines.

The upward bends around $\sigma_{\rm ap}(R_{\rm e}) \approx 140\,{\rm km\,s^{-1}}$ in all of the $M_{\rm BH}$–$\sigma_{\rm ap}(R_{\rm e})$ predictions in Fig. 6 trace back to the peak at $M_{*,\rm tot} \simeq 3.4 \times 10^{10}\ {\rm M}_\odot$ [at $z = 0$; see Fig. 4(b)] in $f_{*,\rm vir}$, the global stellar-to-dark matter mass fraction. Thus, a linear relation $\log(M_{\rm BH}) \sim 4\log(V_{\rm d,pk})$ is strongly distorted by a non-linear 'conversion' from halo circular speeds and virial masses to stellar masses and velocity dispersions. The curves with $2 \leq z_{\rm qso} \leq 4$ in Fig. 6 have average slopes $\Delta\log M_{\rm BH}/\Delta\log\sigma_{\rm ap}(R_{\rm e}) \approx 1.5$–2 for galaxies with $50 \lesssim \sigma_{\rm ap}(R_{\rm e}) \lesssim 100\,{\rm km\,s^{-1}}$, but $\Delta\log M_{\rm BH}/\Delta\log\sigma_{\rm ap}(R_{\rm e}) \approx 5$–7 in the range $200 \lesssim \sigma_{\rm ap}(R_{\rm e}) \lesssim 300\,{\rm km\,s^{-1}}$. However, this curvature is easily accommodated by the data. It is reminiscent of the ad hoc, log-quadratic fits to local M–σ samples by Wyithe (2006a,b, see also Gültekin et al. 2009; McConnell & Ma 2013).

Equally important is the flattening of the model $M_{\rm BH}$–$\sigma_{\rm ap}(R_{\rm e})$ relations away from the $z_{\rm qso} = 0$ curve, which occurs at high $\sigma_{\rm ap}(R_{\rm e}) \gtrsim 300\,{\rm km\,s^{-1}}$ and is more pronounced for larger $z_{\rm qso}$. This is just the behaviour seen in Figs 3 and 5 above: the masses $M_{\rm d,vir}(z)$ and circular speeds $V_{\rm d,pk}(z)$ of the most massive progenitors of haloes (which directly determine $M_{\rm BH}$ here) have flatter dependences at higher z on the final mass $M_{\rm d,vir}(0)$ [related to $\sigma_{\rm ap}(R_{\rm e})$ at $z = 0$ by the scalings of Section 3]. Accounting for the generic redshift evolution of haloes in a ΛCDM cosmology is critical

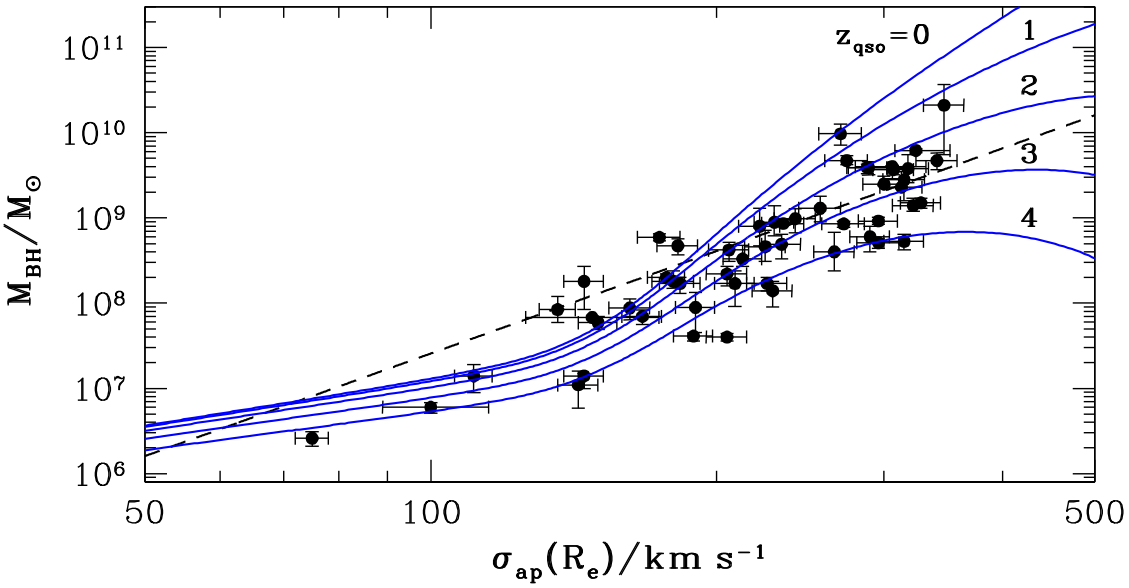

Figure 6. SMBH mass versus stellar velocity dispersion measured inside R_e at $z = 0$. Data points represent the 53 galaxies flagged as early types in McConnell & Ma (2013). The solid blue curves are our models for M_{BH} versus $\sigma_{ap}(R_e)$ at $z = 0$ if a relation $M_{BH} \propto V_{d,pk}^4$ was established by accretion-driven feedback, according to equation (1), at redshift $z_{qso} = 0, 1, 2, 3$ or 4. The curves all assume a Dehnen & McLaughlin (2005) model for the dark-matter halo density profile, and a spatially constant gas-to-dark matter mass ratio $f_0 = 0.18$ in the protogalaxies. They do not include any SMBH growth between $0 < z < z_{qso}$; see the text for discussion. For reference only, the dashed black line shows equation (1) with $V_{d,pk} \equiv \sqrt{2}\,\sigma_{ap}(R_e)$.

to the comparison of models such as equation (1) with data at $z = 0$.

4.2.1 *Dry mergers at low redshift*

It is also in the highest-σ_{ap} regime that gas-poor galaxy mergers at $z < z_{qso}$ may have increased M_{BH} the most from any value determined by quasar-mode feedback at z_{qso}.

Volonteri & Ciotti (2013) perform cosmological simulations of black hole growth in the central galaxies of haloes with masses at $z = 0$ of $10^{13}\ M_\odot \leq M_{d,vir}(0) \leq 10^{15}\ M_\odot$. They track contributions from gas accretion and from SMBH coalescences in gas-poor mergers separately. The results they show for six example haloes with $M_{d,vir}(0) = 10^{15}\ M_\odot$ have the central SMBH growth by accretion essentially finished in all cases at a redshift $z \approx 2$–3. We would associate this here with z_{qso}. Coalescences in dry mergers then drive the growth for $z < z_{qso}$, and especially at $z \lesssim 1$. Ultimately, the SMBH masses are increased by a wide range of factors, $f_{co} \equiv M_{BH}(0)/M_{BH}(z_{qso}) \simeq$ 1–30. For a larger sample of $10^{15}\ M_\odot$ haloes, Volonteri & Ciotti report an average $\langle f_{co}\rangle \approx 11 \pm 10$.

From Section 3, at $z = 0$ the central galaxies in haloes with $M_{d,vir}(0) = 10^{15}\ M_\odot$ typically have $M_{*,tot} \simeq 10^{12}\ M_\odot$ and $\sigma_{ap}(R_e) \approx 350$–$400\ km\ s^{-1}$ (depending on the assumed dark-matter density profile). The rightmost and highest data point in Fig. 6 sits near this region; it represents NGC 4889 in the Coma Cluster, with $\sigma_{ap}(R_e) = 347 \pm 17\ km\ s^{-1}$ (McConnell et al. 2012). This may well be a system where low-redshift merging grew M_{BH} substantially above a feedback-limited value at $z_{qso} = 2$–3.

At lower halo and galaxy masses, there is generally much less SMBH growth through late mergers. For the central galaxies of haloes with $2 \times 10^{13}\ M_\odot \leq M_{d,vir}(0) \leq 10^{14}\ M_\odot$ (corresponding to $M_{*,tot} \simeq 2$–$4 \times 10^{11}\ M_\odot$ and $\sigma_{ap}(R_e) \approx 220$–$275\ km\ s^{-1}$ at $z = 0$), Volonteri & Ciotti give averages of $\langle f_{co}\rangle \approx 2 \pm 1$. For a set of $10^{13}\ M_\odot$ haloes (corresponding to $M_{*,tot} \simeq 1.4 \times 10^{11}\ M_\odot$ and $\sigma_{ap}(R_e) \simeq 200\ km\ s^{-1}$), they find $\langle f_{co}\rangle = 1.8 \pm 1.8$, suggestive of a small systematic effect with a few strong outliers.[2]

Thus, we can expect dry mergers to scatter data *at the top end* of the M–σ relation significantly upwards from curves like those in Fig. 6. This would mask any flattening of the curves at $\sigma_{ap}(R_e) \gtrsim 300\ km\ s^{-1}$ and could appear as a much steeper, even near-vertical mean relation there (the so-called 'saturation' discussed by, e.g., Kormendy & Ho 2013 and McConnell & Ma 2013). Among systems with more moderate velocity dispersions at $z = 0$, dry merging can still introduce some scatter, but not as much. The net shift up from curves for M_{BH} limited by feedback at $z_{qso} \simeq$ 2–3 could plausibly amount to a factor of ≈2–3 in the regime $200 \lesssim \sigma_{ap}(R_e) \lesssim 300\ km\ s^{-1}$, and probably less for lower $\sigma_{ap}(R_e) \lesssim$ 150–200 $km\ s^{-1}$. This should largely preserve the overall shape of such curves.

4.2.2 *Discussion*

Incorporating the generally modest *systematic* effects of low-redshift mergers in the models shown in Fig. 6 would primarily move the curves upwards on the plot. [Mergers at all redshifts are already included in how $V_{d,pk}$ in a progenitor halo at $z_{qso} > 0$ is connected to $\sigma_{ap}(R_e)$ in the central galaxy at $z = 0$; only the value of M_{BH} needs to be adjusted.] However, a few factors could lower the starting M_{BH}–$V_{d,pk}$ relation predicted by equation (1) at any given z_{qso}.

First, if the baryon-to-dark matter mass fraction in a protogalaxy at z_{qso} were less than $f_0 = 0.18$ – the cosmic average, assumed for all of the curves in Fig. 6 – then the critical M_{BH} for blow-out would be decreased proportionately. Secondly, equation (1) ignores any

[2] Volonteri & Ciotti do not show explicitly for any of their haloes with $M_{d,vir}(0) < 10^{15}\ M_\odot$ that accretion-driven growth of the central-galaxy SMBH is negligible after $z_{qso} \approx$ 2–3. However, other simulations imply that this is generally the case (and, indeed, suggest larger z_{qso} in some instances); see, e.g., Sijacki et al. (2007) and Di Matteo et al. (2008).

prior work done by a growing SMBH to push the protogalactic gas outwards before the point of final blow-out, and thus it overestimates the mass required to clear the halo completely at $z_{\rm qso}$. Related to this, lower SMBH masses may suffice to quench quasar-mode accretion by clearing gas from the inner regions to 'far enough' away from a central SMBH, without expelling it fully past the virial radius.

Cosmological simulations are required to evaluate the balance between these effects pushing the model $M_{\rm BH}$–$\sigma_{\rm ap}(R_{\rm e})$ curves downwards in Fig. 6, and the competing effects of late, dry mergers pulling upwards. But at this level, the more fundamental simplifications underlying equation (1) – among others, the idea that quasar-mode feedback is always momentum-driven – need to be improved first.

Likewise, low-redshift mergers are just one possible source of intrinsic *scatter* in the empirical M–σ relation at $z = 0$. Another is different values in different systems for the precise redshift at which the main phase of accretion-driven SMBH growth was ended by quasar-mode feedback. Even if there were a single $z_{\rm qso}$, there must be real scatter in the data around any trend line such as those in Fig. 6, because of the scatter around the constituent scalings from Sections 2 and 3 for haloes, halo evolution and central galaxies. It is important, but beyond the scope of this paper, to understand the physical content of the observed M–σ scatter in detail. Part of the challenge is to know the 'correct' trend for $M_{\rm BH}$ versus $\sigma_{\rm ap}(R_{\rm e})$ at $z = 0$, around which scatter should be calculated. In the context of feedback models, this again requires improving on equation (1) for the prediction of $M_{\rm BH}$ values at $z_{\rm qso} > 0$.

5 SUMMARY

We have examined how a simple relationship between SMBH masses $M_{\rm BH}$ and the circular speeds $V_{\rm d,pk}$ in protogalactic dark-matter haloes, established by quasar-mode feedback at redshift $z_{\rm qso} > 0$, is reflected in a correlation between $M_{\rm BH}$ and the stellar velocity dispersions $\sigma_{\rm ap}(R_{\rm e})$ in early-type galaxies at $z = 0$. Straightforward but non-trivial approximations for halo growth and scalings between haloes and their central galaxies transform a power-law $M_{\rm BH}$–$V_{\rm d,pk}$ relation at $z_{\rm qso}$ into a decidedly *non*-power-law $M_{\rm BH}$–$\sigma_{\rm ap}(R_{\rm e})$ relation at $z = 0$. This relation nevertheless compares well to current data, for assumed values of $z_{\rm qso} \approx 2$–4.

We worked with two-component models for spherical galaxies. Because the stellar properties most relevant to us are those at (or averaged inside) an effective radius, it sufficed to assume Hernquist (1990) density profiles for the stars inside any galaxy. Because dark-matter haloes are key to determining SMBH mass in the feedback scenario we focused on, we allowed for any of four different halo density profiles: those of Navarro et al. (1996, 1997), Hernquist (1990), Dehnen & McLaughlin (2005) and Burkert (1995).

The scaling relations we developed are trend lines connecting average stellar properties at $z = 0$ [total masses $M_{*,\rm tot}$, effective radii $R_{\rm e}$, aperture velocity dispersions $\sigma_{\rm ap}(R_{\rm e})$ and dark-matter mass fractions] to the typical virial masses $M_{\rm d,vir}$ and peak circular speeds $V_{\rm d,pk}$ of dark-matter haloes at $z = 0$ *and* their most massive progenitors up to $z \lesssim 4$–5. These scalings are constrained by theoretical work in the literature on the global structures, baryon contents and redshift evolution of dark-matter haloes (Section 2) and by data in the literature for local elliptical galaxies (Section 3). They are robust for normal early-type systems with stellar masses greater than several $\times\ 10^9$ M$_\odot$ at $z = 0$, corresponding to velocity dispersions $\sigma_{\rm ap}(R_{\rm e}) \gtrsim 60$–70 km s^{-1}, but are largely untested against lower mass dwarf galaxies (see Section 3.6).

We applied the scalings to show in Section 4 how a relationship of the form $M_{\rm BH} \propto V_{\rm d,pk}^4$ at a range of redshifts $z_{\rm qso} > 0$ (equation 1; McQuillin & McLaughlin 2012) appears as a much more complicated $M_{\rm BH}$–$\sigma_{\rm ap}(R_{\rm e})$ relation at $z = 0$. The specific form for an initial $M_{\rm BH}$–$V_{\rm d,pk}$ relation comes from a simplified theoretical analysis of *momentum-conserving* SMBH feedback in *isolated and virialized* gaseous protogalaxies with *non-isothermal* dark-matter haloes. Some of the simplifying assumptions involved thus need to be relaxed and improved in future work. Meanwhile, the highly 'non-linear' observable $M_{\rm BH}$–$\sigma_{\rm ap}(R_{\rm e})$ relation we infer from it does describe the data for local early types if the redshift of quasar-mode blow-out was $z_{\rm qso} \approx 2$–4. This range is reassuringly similar to the epoch of peak quasar density and SMBH accretion rate in the Universe.

This lends support to the notion that the empirical M–σ relation fundamentally reflects *some* close connection due to accretion feedback between SMBH masses in galactic nuclei and the *dark matter* in their host (proto)galaxies. It also demonstrates that the true, physical relationship between $M_{\rm BH}$ and stellar velocity dispersion at $z = 0$ is not necessarily a pure power law. The shape in our analysis has an upward bend around $\sigma_{\rm ap}(R_{\rm e}) \approx 140$ km s^{-1} (Fig. 6), corresponding to stellar masses $M_{*,\rm tot} \approx 3$–4×10^{10} M$_\odot$ and halo masses $M_{\rm d,vir}(0) \approx 10^{12}$ M$_\odot$ at $z = 0$. This bend comes from a sharp maximum at these masses in the global stellar-to-dark matter fractions, $M_{*,\rm tot}/M_{\rm d,vir}(0)$ (e.g. Moster et al. 2010). Consequently, there is a sharp upturn in the dependence of halo circular speeds $V_{\rm d,pk}$ on the stellar $\sigma_{\rm ap}(R_{\rm e})$ (see Figs 4 and 5).

Our models also show a flattening of $M_{\rm BH}$ versus $\sigma_{\rm ap}(R_{\rm e})$ at $z = 0$ for velocity dispersions above 300 km s^{-1} or so, for any blow-out redshift $z_{\rm qso} > 0$ but more so for higher $z_{\rm qso}$ (Fig. 6). This is due to the way that dark-matter halo masses grow and circular speeds increase through hierarchical merging in a ΛCDM cosmology after $M_{\rm BH}$ is set by feedback and the halo properties at $z_{\rm qso}$ (see Fig. 3). However, the values we calculate for $M_{\rm BH}$ include only the growth by accretion up to $z = z_{\rm qso}$; further growth through SMBH–SMBH coalescences in gas-poor mergers at lower redshifts is neglected. (The effects of such mergers on halo masses and circular speeds, and stellar velocity dispersions at $z = 0$, *are* accounted for.)

As discussed in Section 4.2, simulations by Volonteri & Ciotti (2013) suggest that low-redshift merging has a significant effect on the SMBH masses in systems with large $\sigma_{\rm ap}(R_{\rm e}) \gtrsim 300$–350 km s^{-1} at $z = 0$. There, dry mergers can scatter $M_{\rm BH}$ values strongly upwards from the values at $z_{\rm qso}$, essentially erasing the flattening that might otherwise be observed at $z = 0$ and 'saturating' the empirical M–σ relation. In galaxies with lower $\sigma_{\rm ap}(R_{\rm e}) \lesssim 300$ km s^{-1}, where most current data fall, such scatter up from feedback-limited SMBH masses will be much more modest in general. The expected $M_{\rm BH}$–$\sigma_{\rm ap}(R_{\rm e})$ relations at $z = 0$ should then have the same basic shape as when late mergers are ignored.

Although we have focused on the observed M–σ relation, other SMBH–bulge correlations exist that may be just as strong intrinsically. These include the $M_{\rm BH}$–$M_{\rm bulge}$ correlation and multivariate, 'fundamental-plane' relationships between $M_{\rm BH}$ and non-trivial combinations of $M_{*,\rm tot}$, $R_{\rm e}$ and $\sigma_{\rm ap}(R_{\rm e})$. They should also reflect any underlying SMBH–dark matter connection at some $z_{\rm qso} > 0$, and the techniques of this paper can be applied to look at them as well. However, this will best be done with close attention also paid to the inevitable scatter around all of the scalings we have adopted for both stellar and dark-matter halo properties. It remains to be understood how the numerous individual sources of scatter combine to produce SMBH correlations with apparently so little net scatter at $z = 0$.

More sophisticated predictions of critical SMBH masses for quasar-mode blow-out in terms of protogalactic dark-matter halo properties are required. The simple relation $M_{\rm BH} \propto V_{\rm d,pk}^4$ that we have used makes very specific assumptions about the mechanism (e.g. momentum-driven) and the setting (spherical protogalaxies with no stars, initially virialized gas, smooth outflows) of the feedback that establishes it. We mentioned in Sections 1.1 and 4.2 several ways to improve on these assumptions. Our work in this paper is readily adaptable to help test any refinements.

ACKNOWLEDGEMENTS

ACL has been supported by an STFC studentship.

REFERENCES

Behroozi P. S., Wechsler R. H., Conroy C., 2013, ApJ, 770, 57
Blakeslee J. P. et al., 2009, ApJ, 694, 556
Bruzual G., Charlot S., 2003, MNRAS, 344, 1000
Bryan G. L., Norman M. L., 1998, ApJ, 495, 80
Bullock J. S., Kolatt T. S., Sigad Y., Somerville R. S., Kravtsov A. V., Klypin A. A., Primack J. R., Dekel A., 2001, MNRAS, 321, 559
Burkert A., 1995, ApJ, 447, L25
Burkert A., Silk J., 1997, ApJ, 488, L55
Cappellari M. et al., 2011, MNRAS, 413, 813
Cappellari M. et al., 2013a, MNRAS, 432, 1709
Cappellari M. et al., 2013b, MNRAS, 432, 1862
Chen C.-W., Côté P., West A. A., Peng E. W., Ferrarese L., 2010, ApJ, 191, 1
Costa T., Sijacki D., Haehnelt M. G., 2014, MNRAS, 444, 2355
Côté P. et al., 2001, ApJ, 559, 828
Côté P., McLaughlin D. E., Cohen J. G., Blakeslee J. P., 2003, ApJ, 591, 850
Côté P. et al., 2004, ApJS, 153, 223
Dehnen W., McLaughlin D. E., 2005, MNRAS, 362, 1057
Dehnen W., McLaughlin D. E., Sachania J., 2006, MNRAS, 369, 1688
Delvecchio I. et al., 2014, MNRAS, 439, 2736
Di Matteo T., Colberg J., Springel V., Hernquist L., Sijacki D., 2008, ApJ, 676, 33
Dubinski J., Carlberg R. G., 1991, ApJ, 378, 496
Dutton A., Macciò A., 2014, MNRAS, 441, 3359
Einasto J., 1965, Tr. Astrofiz. Inst. Alma-Ata, 5, 87
Fabian A. C., 1999, MNRAS, 308, L39
Ferrarese L., Ford H., 2005, Space Sci. Rev., 116, 523
Ferrarese L., Merritt D., 2000, ApJ, 539, L9
Freeman K. C., 1985, in van Woerden H., Allen R. J., Burton W. B., eds, Proc. IAU Symp. 106, The Milky Way Galaxy. Reidel, Dordrecht, p. 113
Gebhardt K. et al., 2000, ApJ, 539, L13
Giodini S. et al., 2009, ApJ, 703, 982
Gonzalez A. H., Sivanandam S., Zabludoff A. I., Zaritsky D., 2013, ApJ, 778, 14
Graham A., Colless M., 1997, MNRAS, 287, 221
Graham A. W., Merritt D., More B., Diemand J., Terzic B., 2006, AJ, 132, 2711
Gültekin K. et al., 2009, ApJ, 698, 198
Häring N., Rix H.-W., 2004, ApJ, 604, L89
Hernquist L., 1990, ApJ, 356, 359
Hopkins P. F., Richards G. T., Hernquist L., 2007a, ApJ, 654, 731
Hopkins P. F., Hernquist L., Cox T. J., Robertson B., Krause E., 2007b, ApJ, 669, 45
Hopkins P. F., Hernquist L., Cox T. J., Robertson B., Krause E., 2007c, ApJ, 669, 67
King A., 2003, ApJ, 596, L27
King A., 2005, ApJ, 635, L121
King A., 2010, MNRAS, 402, 1516
King A., Pounds K. A., 2003, MNRAS, 345, 657
Kormendy J., Ho L. C., 2013, ARA&A, 51, 511
Kroupa P., 2001, MNRAS, 322, 231
Łokas E. L., Mamon G. A., 2003, MNRAS, 343, 401
McConnell N. J., Ma C.-P., 2013, ApJ, 764, 184
McConnell N. J., Ma C.-P., Gebhardt K., Wright S. A., Murphy J. D., Lauer T. R., Graham J. R., Richstone D. O., 2011, Nature, 480, 215
McConnell N. J., Ma C.-P., Murphy J. D., Gebhardt K., Lauer T. R., Graham J. R., Wright S. A., Richstone D. O., 2012, ApJ, 756, 179
McGaugh S. S., Schombert J. M., de Blok W. J. G., Zagursky M. J., 2010, ApJ, 708, L14
McLaughlin D. E., 1999, ApJ, 512, L9
McMillan P. J., 2011, MNRAS, 414, 2446
McQuillin R. C., McLaughlin D. E., 2012, MNRAS, 423, 2162
McQuillin R. C., McLaughlin D. E., 2013, MNRAS, 434, 1332
Magorrian J. et al., 1998, AJ, 115, 2285
Maraston C., 1998, MNRAS, 300, 872
Maraston C., 2005, MNRAS, 362, 799
Marconi A., Hunt L. K., 2003, ApJ, 589, L21
Moster B., Somerville R. S., Maulbetsch C., van den Bosch F. C., Macciò A. V., Naab T., Oser L., 2010, ApJ, 710, 903
Murray N., Quataert E., Thompson T. A., 2005, ApJ, 618, 569
Navarro J. F., Frenk C. S., White S. D. M., 1996, ApJ, 462, 563
Navarro J. F., Frenk C. S., White S. D. M., 1997, ApJ, 490, 493
Planck Collaboration XVI, 2014, A&A, 571, A16
Pontzen A., Governato F., 2012, MNRAS, 421, 3464
Pounds K. A., Reeves J. N., King A. R., Page K. L., O'Brien P. T., Turner M. J. L., 2003, MNRAS, 345, 705
Power C., Zubovas K., Nayakshin S., King A. R., 2011, MNRAS, 413, L110
Reeves J. N., O'Brien P. T., Ward M. J., 2003, ApJ, 593, L65
Richards G. T. et al., 2006, AJ, 131, 2766
Sérsic J.-L., 1968, Atlas de Galaxias Astrales. Observatorio Astronomico, Cordoba
Shankar F. et al., 2016, MNRAS, 460, 3119
Sijacki D., Springel V., Di Matteo T., Hernquist L., 2007, MNRAS, 380, 877
Sijacki D., Voglesberger M., Genel S., Springel V., Torrey P., Snyder G. F., Nelson D., Hernquist L., 2015, MNRAS, 452, 575
Silk J., Rees M. J., 1998, A&A, 331, L1
Tombesi F., Cappi M., Reeves J. N., Palumbo G. G. C., Yaqoob T., Braito V., Dadina M., 2010, A&A, 521, A57
Tombesi F., Cappi M., Reeves J. N., Palumbo G. G. C., Braito V., Dadina M., 2011, ApJ, 742, 44
van den Bosch F. C., Jiang F., Hearin A., Campbell D., Watson D., Padmanabhan N., 2014, MNRAS, 445, 1713
Volonteri M., Ciotti L., 2013, ApJ, 768, 29
Wyithe S. B., 2006a, MNRAS, 365, 1082
Wyithe S. B., 2006b, MNRAS, 371, 1536
Yu Q., Tremaine S., 2002, MNRAS, 335, 965
Zhang Y. Y., Laganá T. F., Pierini D., Puchwein E., Schneider P., Reiprich T. H., 2011, A&A, 535, A78
Zhao D. H., Jing Y. P., Mo H. J., Börner G., 2009, ApJ, 707, 354
Zubovas K., King A., 2012, MNRAS, 426, 2751
Zubovas K., Nayakshin S., 2014, MNRAS, 440, 2625

APPENDIX A: MODEL CHECKS AT $z = 0$

Here we collect some properties from the literature for a few galaxies and haloes spanning the range of mass and stellar velocity dispersion covered by local galaxy samples used to define empirical SMBH M–σ relations. We then extract numerical values from the $z = 0$ scalings in Section 3 (Fig. 4) to compare with the measurements.

A1 Stellar and halo properties from the literature

Table A1 lists observed stellar properties of the Milky Way, M87 (at the centre of Virgo subcluster A), M49 (at the centre of Virgo B)

Table A1. Values of stellar and dark-matter halo properties at $z = 0$, taken from various sources in the literature. References: 1 – McMillan (2011), 2 – Freeman (1985), 3 – McConnell & Ma (2013), 4 – Cappellari et al. (2011), 5 – Cappellari et al. (2013a), 6 – McLaughlin (1999), 7 – Côté et al. (2001), 8 – Chen et al. (2010), 9 – Côté et al. (2003), 10 – McConnell et al. (2011, 2012), 11 – Łokas & Mamon (2003).

Galaxy	$M_{*,\rm tot}$ ($\rm M_\odot$)	$R_{\rm e}$ (kpc)	ref.	$\sigma_{\rm ap}(R_{\rm e})$ ($\rm km\,s^{-1}$)	ref.	$V_{\rm d,pk}$ ($\rm km\,s^{-1}$)	$r_{\rm pk}$ (kpc)	$M_{\rm d,200}$ or $M_{\rm d,vir}$ ($\rm M_\odot$)	r_{200} or $r_{\rm vir}$ (kpc)	ref.
Milky Way	6.4×10^{10}	–	1	–	–	185	52	1.26×10^{12}	230	1
MW bulge	9.0×10^{9}	2.7 ± 0.3	1,2	103 ± 20	3	–	–	–	–	–
M87	2.9×10^{11}	6.8 ± 1.5	4	264 ± 13	5	1100	1200	4.2×10^{14}	1550	6,7
	3.2×10^{11}	8.7 ± 1.1	8	–	–	–	–	–	–	–
	3.7×10^{11}	–	3	324^{+28}_{-16}	3	–	–	–	–	–
M49	4.2×10^{11}	7.9 ± 1.7	4	250 ± 13	5	710	425	9.4×10^{13}	950	9
	4.7×10^{11}	13.4 ± 1.1	8	–	–	–	–	–	–	–
	3.7×10^{11}	–	3	300 ± 15	3	–	–	–	–	–
NGC 4889	9.5×10^{11}	27 ± 2	3,10	347 ± 17	3,10	1585	670	1.2×10^{15}	2900	11

and NGC 4889 (in the Coma Cluster). Properties of the dark-matter haloes are also given, from dynamical modelling in the literature. Our analysis is clearly not meant to describe disc galaxies, but we have included the Milky Way as a useful check on the implications for $\sim L^\star$ galaxies in general.

A1.1 The Milky Way

In the first row of Table A1, the total stellar mass, the radius r_{200} of mean overdensity $\Delta \equiv 200$ and the dark-matter mass $M_{\rm d,200}$ inside this are all taken from McMillan (2011). Combining his best-fitting NFW concentration, $r_{200}/r_{-2} \simeq 9.55$, with his values of $M_{\rm d,200}$ and r_{200} plus $r_{\rm pk}/r_{-2} = 2.16258$ for an NFW halo yields $r_{\rm pk} \simeq 52\,\rm kpc$ and $V_{\rm d,pk} \simeq 185\,\rm km\,s^{-1}$. These are consistent with separate modelling of the Milky Way by Dehnen, McLaughlin & Sachania (2006).

The second row of Table A1 contains the total stellar mass of the Milky Way bulge only, according to McMillan (2011). He does not record the effective radius of the bulge or the aperture dispersion inside it, so we take $R_{\rm e} \simeq 2.7\,\rm kpc$ from Freeman (1985) and $\sigma_{\rm ap}(R_{\rm e}) \simeq 103\ \rm km\,s^{-1}$ from McConnell & Ma (2013).

A1.2 M87 and M49

For M87 and M49, Table A1 quotes total stellar masses based on three different sources: the ATLAS$^{\rm 3D}$ survey (Cappellari et al. 2011), the ACSVCS (Chen et al. 2010) and McConnell & Ma (2013). The original authors give total luminosities, to which we have applied mass-to-light ratios from Maraston (2005) models for a Kroupa (2001) IMF and a stellar age of 9 Gyr: $M_{*,\rm tot}/L_K \simeq 0.88\,\rm M_\odot\ L_\odot^{-1}$ for the ATLAS$^{\rm 3D}$ luminosity, $M_{*,\rm tot}/L_z \simeq 1.7\,\rm M_\odot\ L_\odot^{-1}$ for the ACSVCS value and $M_{*,\rm tot}/L_V \approx 3.15\,\rm M_\odot\ L_\odot^{-1}$ for McConnell & Ma (2013). Both galaxies have $R_{\rm e}$ values in the ATLAS$^{\rm 3D}$ survey and the ACSVCS, and velocity dispersions in ATLAS and McConnell & Ma (2013).

McLaughlin (1999) and Côté et al. (2001) fitted the kinematics of stars and globular clusters in M87, plus the kinematics of Virgo-cluster galaxies and the total mass profile derived from intracluster X-ray gas, with a two-component mass model comprising the stars (plus remnants and stellar ejecta) in the body of M87 and an NFW dark-matter halo with $r_{200} \simeq 1.55\,\rm Mpc$ and $M_{\rm d,200} \simeq 4.2 \times 10^{14}\,\rm M_\odot$. This clearly identifies the dark matter in and around M87 with the halo of the entire Virgo A subcluster. McLaughlin and Côté et al. have an NFW concentration of $r_{200}/r_{-2} = 2.8 \pm 0.7$ for the M87/Virgo A halo, so (with $r_{\rm pk}/r_{-2} = 2.162\,58$ again) $r_{\rm pk} \sim 1.2\,\rm Mpc$ and $V_{\rm d,pk} \simeq 1100\,\rm km\,s^{-1}$.

For M49/Virgo B, Côté et al. (2003) similarly use a two-component mass model consisting of the galaxy's stars plus a single NFW dark-matter halo, to fit the stellar and globular cluster kinematics on $\lesssim$50 kpc scales and the X-ray mass profile out to ~Mpc radii. The Côté et al. analysis implies $r_{200} \simeq 950\,\rm kpc$ with $M_{\rm d,200} \simeq 9.4 \times 10^{13}\,\rm M_\odot$, and $r_{200}/r_{-2} \simeq 4.8$. The dark-matter circular speed therefore peaks at $r_{\rm pk} \simeq 425\,\rm kpc$, where $V_{\rm d,pk} \simeq 710\,\rm km\,s^{-1}$.

A1.3 NGC 4889

NGC 4889 is the brightest galaxy in Coma and not far from the nominal central galaxy, NGC 4874. According to McConnell & Ma (2013), NGC 4889 has $L_V \simeq 3.0 \times 10^{11}\,\rm L_\odot$ and hence [for $M_*/L_V \approx 3.15\,\rm M_\odot\ L_\odot^{-1}$ from the Maraston (2005) population-synthesis models] $M_{*,\rm tot} \approx 9.5 \times 10^{11}\,\rm M_\odot$. It is at the uppermost end of the range of stellar masses plotted for our relations in Fig. 4 (but it does not appear on those plots since it is not in the ATLAS$^{\rm 3D}$ survey), and it hosts one of the largest SMBHs yet measured: $M_{\rm BH} = (2.1 \pm 1.6) \times 10^{10}\,\rm M_\odot$ (McConnell et al. 2011, 2012). The effective radius $R_{\rm e} = 27\,\rm kpc$ and velocity dispersion $\sigma_{\rm ap}(R_{\rm e}) = 347\,\rm km\,s^{-1}$ in Table A1 are from McConnell & Ma (2013) and McConnell et al. (2011, 2012).

The global dark-matter properties of the Coma Cluster are taken from dynamical modelling by Łokas & Mamon (2003). They give values for $r_{\rm vir}$ and $M_{\rm d,vir}$, rather than r_{200} and $M_{\rm d,200}$ like the other galaxies in Table A1, and a best-fitting NFW concentration of $r_{\rm vir}/r_{-2} = 9.4$. Together these imply $r_{\rm pk} \simeq 670\,\rm kpc$ and $V_{\rm d,pk} \simeq 1585\,\rm km\,s^{-1}$.

A2 Comparison to models

Taking the total stellar mass $M_{*,\rm tot}$ as a starting point for each of the systems in Table A1, we now find their other stellar and halo properties from the scaling relations developed in Section 3. Table A2 shows the results for $R_{\rm e}$, $\sigma_{\rm ap}(R_{\rm e})$, $V_{\rm d,pk}$, $r_{\rm pk}$, $M_{\rm d,200}$ or (for NGC 4889/Coma) $M_{\rm d,vir}$, and r_{200} or (for NGC 4889/Coma) $r_{\rm vir}$.

A2.1 L* galaxies: $\sigma_{\rm ap}(R_{\rm e}) \sim$ 100–150 km s^{-1}

For $M_{*,\rm tot} \simeq 6.4 \times 10^{10}\,\rm M_\odot$ (the *total* Milky Way mass), our scalings give the stellar effective radius as $R_{\rm e} \simeq 3\,\rm kpc$ and the velocity dispersion as $\sigma_{\rm ap}(R_{\rm e}) \simeq 160\,\rm km\,s^{-1}$. This dispersion is rather higher than the value typically used to put the Milky Way on the black hole

Table A2. Stellar and dark-matter halo properties at $z = 0$ according to our scaling relations. For each galaxy, the starting point is $M_{*,\rm tot}$, taken from the literature.

Galaxy	$M_{*,\rm tot}$ ($\rm M_\odot$)	$R_{\rm e}$ (kpc)	$\sigma_{\rm ap}(R_{\rm e})$ ($\rm km\,s^{-1}$)	$V_{\rm d,pk}$ ($\rm km\,s^{-1}$)	$r_{\rm pk}$ (kpc)	$M_{\rm d,200}$ or $M_{\rm d,vir}$ ($\rm M_\odot$)	r_{200} or $r_{\rm vir}$ (kpc)
Milky Way	6.4×10^{10}	3.0	160	200	75	2.0×10^{12}	270
MW bulge	9.0×10^{9}	1.4	90	120	35	3.6×10^{11}	150
M87	3.3×10^{11}	8.0	245	600	330	6.0×10^{13}	830
M49	4.2×10^{11}	9.3	265	720	420	1.0×10^{14}	1000
NGC 4889	9.5×10^{11}	15.2	345	1285	925	8.0×10^{14}	2450

M–σ relation: for example, McConnell & Ma (2013) take $\sigma_{\rm ap}(R_{\rm e}) = 103\,\rm km\,s^{-1}$ for the Galaxy. However, this value is meant to represent the bulge only. For the *bulge* mass of $M_{*,\rm tot} \simeq 9 \times 10^9\,\rm M_\odot$, our relations give $R_{\rm e} \simeq 1.4$ kpc and $\sigma_{\rm ap}(R_{\rm e}) \simeq 90\,\rm km\,s^{-1}$.

For the total Galactic stellar mass of $6.4 \times 10^{10}\,\rm M_\odot$ and assuming an NFW halo, the scalings lead to a peak circular speed of $V_{\rm d,pk} \simeq 200\,\rm km\,s^{-1}$, occurring at $r_{\rm pk} \simeq 75$ kpc. Using equations (5), (24) and (23) to go from the virial radius implied by $M_{*,\rm tot}$ to the radius of mean overdensity $\Delta = 200$, we find $M_{\rm d,200} \simeq 2 \times 10^{12}\,\rm M_\odot$ and $r_{200} \simeq 270$ kpc. For the mass of the bulge alone, $M_{*,\rm tot} \simeq 9 \times 10^9\,\rm M_\odot$, we obtain $V_{\rm d,pk} \sim 120\,\rm km\,s^{-1}$, $r_{\rm pk} \sim 35$ kpc, $M_{\rm d,200} \sim 3.6 \times 10^{11}\,\rm M_\odot$ and $r_{200} \sim 150$ kpc.

A2.2 M87 and M49: $\sigma_{\rm ap}(\rm R_e) \sim 250\,km\,s^{-1}$

For each of these galaxies, we take the mean of $M_{*,\rm tot}$ from the three different values in Table A1. Thus, $M_{*,\rm tot} = 3.3 \times 10^{11}\,\rm M_\odot$ for M87, and $M_{*,\rm tot} = 4.2 \times 10^{11}\,\rm M_\odot$ for M49. Our parametrization of $R_{\rm e}$ versus $M_{*,\rm tot}$ in Section 3.1 then gives the values recorded in Table A2, which broadly agree with the measurements of $R_{\rm e}$. The model values in Table A2 for $\sigma_{\rm ap}(R_{\rm e})$, $V_{\rm d,pk}$, $r_{\rm pk}$, $M_{\rm d,200}$ and r_{200} assume an NFW halo around each galaxy (as the analyses from the literature do). The predicted velocity dispersions compare well to the measurements for M87 and M49 in the ATLAS$^{\rm 3D}$ survey but not quite as well to the values recorded by McConnell & Ma (2013), which are 20 per cent higher.

The value of r_{200} for M87/Virgo A in Table A1, from McLaughlin (1999), is $\simeq 80$ per cent bigger than the one in Table A2, implied by our models here. McLaughlin's $M_{\rm d,200}$ is consequently larger by about a factor of $1.8^3 \simeq 6$. Similarly, the circular-speed curve of the halo in McLaughlin (1999) peaks at $r_{\rm pk} \sim 1.2$ Mpc (with a very large uncertainty) rather than $r_{\rm pk} \simeq 330$ kpc as expected here, and it has $V_{\rm d,pk} \simeq 1100\,\rm km\,s^{-1}$ rather than $V_{\rm d,pk} \simeq 600\,\rm km\,s^{-1}$.

These discrepancies for M87/Virgo A may simply reflect the inevitable scatter in the properties of individual systems around the typical values given by our trend lines. For M49/Virgo B, all of the halo properties in Table A2 obtained from our scalings are remarkably close to the values in Table A1 from Côté et al. (2003).

A2.3 NGC 4889: $\sigma_{\rm ap}(R_{\rm e}) \sim 350\,km\,s^{-1}$

For $M_{*,\rm tot} = 9.5 \times 10^{11}\,\rm M_\odot$, our scalings give $R_{\rm e} = 15.2$ kpc and (assuming an NFW halo) $\sigma_{\rm ap}(R_{\rm e}) \simeq 345\,\rm km\,s^{-1}$. The velocity dispersion agrees with the value in McConnell et al. (2011, 2012), although the effective radius is smaller than their adopted 27 kpc. Further, we find $r_{\rm vir} \simeq 2.45$ Mpc and $M_{\rm d,vir} \simeq 8.0 \times 10^{14}\,\rm M_\odot$, which compare well to the values in Table A1 determined by Łokas & Mamon (2003). (This is even though NGC 4889 is not precisely at the centre of the Coma Cluster.)

Assuming an NFW halo density profile, our models imply $r_{\rm pk} \simeq 925$ kpc and $V_{\rm d,pk} \simeq 1285\,\rm km\,s^{-1}$ for the peak of the dark-matter circular speed in NGC 4889/Coma – different by ~ 30 per cent from the Łokas & Mamon numbers. Comparing to the peak radii and speeds above for M87/Virgo A and M49/Virgo B emphasizes the clear visual impression given by Fig. 4. In large galaxies $V_{\rm d,pk}$, along with $M_{\rm d,vir}$, is a much more sensitive function of galaxy stellar mass than the stellar $\sigma_{\rm ap}(R_{\rm e})$ is. [This follows directly from the steep decline at high masses in the cosmological connection between $M_{*,\rm tot}$ and $M_{\rm d,vir}$ adopted from Moster et al. (2010).] It therefore seems natural to expect much more scatter and many more apparent 'outliers' in $M_{\rm BH}$ among very massive galaxies, if SMBH masses are connected fundamentally to the global properties of dark-matter haloes rather than to stellar velocity dispersions directly.

This paper has been typeset from a TEX/LATEX file prepared by the author.